

## **SANDIA REPORT**

SAND2016-11612

Unlimited Release

Printed November 2016

# **Fundamental Scaling of Microplasmas and Tunable UV Light Generation**

Ronald P. Manginell, Colin H. Sillerud, Matthew Hopkins, Benjamin Yee, Matthew Moorman Peter D.D. Schwindt, John M. Anderson and Nathaniel B. Pfeifer

Prepared by  
Sandia National Laboratories  
Albuquerque, New Mexico 87185 and Livermore, California 94550

Sandia National Laboratories is a multi-mission laboratory managed and operated by Sandia Corporation, a wholly owned subsidiary of Lockheed Martin Corporation, for the U.S. Department of Energy's National Nuclear Security Administration under contract DE-AC04-94AL85000.

Approved for public release; further dissemination unlimited.



**Sandia National Laboratories**

Issued by Sandia National Laboratories, operated for the United States Department of Energy by Sandia Corporation.

**NOTICE:** This report was prepared as an account of work sponsored by an agency of the United States Government. Neither the United States Government, nor any agency thereof, nor any of their employees, nor any of their contractors, subcontractors, or their employees, make any warranty, express or implied, or assume any legal liability or responsibility for the accuracy, completeness, or usefulness of any information, apparatus, product, or process disclosed, or represent that its use would not infringe privately owned rights. Reference herein to any specific commercial product, process, or service by trade name, trademark, manufacturer, or otherwise, does not necessarily constitute or imply its endorsement, recommendation, or favoring by the United States Government, any agency thereof, or any of their contractors or subcontractors. The views and opinions expressed herein do not necessarily state or reflect those of the United States Government, any agency thereof, or any of their contractors.

Printed in the United States of America. This report has been reproduced directly from the best available copy.

Available to DOE and DOE contractors from

U.S. Department of Energy  
Office of Scientific and Technical Information  
P.O. Box 62  
Oak Ridge, TN 37831

Telephone: (865) 576-8401  
Facsimile: (865) 576-5728  
E-Mail: [reports@osti.gov](mailto:reports@osti.gov)  
Online ordering: <http://www.osti.gov/scitech>

Available to the public from

U.S. Department of Commerce  
National Technical Information Service  
5301 Shawnee Rd  
Alexandria, VA 22312

Telephone: (800) 553-6847  
Facsimile: (703) 605-6900  
E-Mail: [orders@ntis.gov](mailto:orders@ntis.gov)  
Online order: <http://www.ntis.gov/search>



# Fundamental Scaling of Microplasmas and Tunable UV Light Generation

<sup>1</sup>Ronald P. Manginell, <sup>1</sup>John M. Anderson, <sup>4</sup>E. H. Dirk, <sup>3</sup>Matthew Hopkins, <sup>1</sup>Matthew W. Moorman, <sup>1</sup>Nathaniel B. Pfeifer, <sup>2</sup>Peter D. D. Schwindt, <sup>1</sup>Colin H. Sillerud, <sup>3</sup>Benjamin T. Yee

<sup>1</sup>Nano and Micro Sensors Department  
<sup>2</sup>Physics Based Microsystems Department  
<sup>3</sup>Applied Optical/Plasma Science Department  
Sandia National Laboratories  
P.O. Box 5800  
Albuquerque, New Mexico 87185-MS0892

<sup>4</sup>Department of Chemical and Biological Engineering  
The University of New Mexico  
MSC01 1120  
Albuquerque, New Mexico 87131

## Abstract

The temporal evolution of spectral lines from microplasma devices (MD) was studied, including impurity transitions. Long-wavelength emission diminishes more rapidly than deep UV with decreasing pulse width and RF operation. Thus, switching from DC to short pulsed or RF operation, UV emissions can be suppressed, allowing for real-time tuning of the ionization energy of a microplasma photo-ionization source, which is useful for chemical and atomic physics. Scaling allows MD to operate near atmospheric pressure where excimer states are efficiently created and emit down to 65 nm; laser emissions fall off below 200 nm, making MD light sources attractive for deep UV use. A first fully-kinetic three-dimensional model was developed that explicitly calculates electron-energy distribution function. This, and non-continuum effects, were studied with the model and how they are impacted by geometry and transient or DC operation. Finally, a global non-dimensional model was developed to help explain general trends MD physics.

## ACKNOWLEDGMENTS

Sandia National Laboratories is a multi-mission laboratory managed and operated by Sandia Corporation, a wholly owned subsidiary of Lockheed Martin Corporation, for the U.S. Department of Energy's national Nuclear Security Administration under contract DE-AC04-94AL85000. The authors would like to gratefully acknowledge the following individuals: Douglas Read for instrumentation and Labview programming; Juan-Elizondo Decanini for high-speed measurement assistance; Mike Mangan for measurement advice and loaning of test equipment and vacuum pumps; Chris Moore and Jeremy Boerner for modeling advice and manuscript review; Kathy Myers for device packaging and wirebonding; Andy Fierro and George Laity for discussions on plasma theory and pulsing techniques; Pat Lake and Mark Johnston for invaluable assistance with spectrometry; Todd Barrick for vacuum equipment installation; Al Staton for hardware installation; Wahid Hermina, Steve Casalnuovo, Mary Crawford and Sandia's LDRD office for funding this work.

## CONTENTS

1. Introduction.....	9
2. Spectra of nanosecond pulsed md in neon.....	11
2.1. Introduction.....	11
2.1. Microplasma device array fabrication testing and failure analysis .....	12
2.1.1 Fabrication.....	12
2.1.2 Testing in DC and Pulsed Modes.....	12
2.2. Experimental Apparatus .....	14
2.3 Global Model .....	15
2.4 Results.....	17
2.4.1 Electrical Characteristics.....	17
2.4.2 Chamber Gas .....	19
2.4.3 Optical Traces .....	19
2.4.4 Integrated Emissions .....	22
2.5 Conclusions.....	26
2.6 References for Section 2 .....	26
3. RF operation .....	31
4. 3D Fully Kinetic Simulation of Microscale Discharge .....	37
4.1 Introduction.....	37
4.2 Model Description .....	38
4.2.1 Physical System .....	38
4.2.2 Geometry and Mesh Resolution.....	39
4.2.3 Temporal Resolution.....	41
4.2.4 Plasma Chemistry.....	42
4.2.5 Initial Condition .....	43
4.2.6 Boundary Condition .....	43
4.2.7 Particle Weights .....	44
4.3 Results and Discussion .....	45
4.4 Conclusions of the 3D Model and Simulation.....	52
4.5 References for Section 4 .....	53
5. Conclusions.....	54
Appendix1: Global Model .....	57
A1.1 Model Equations .....	57
A1.1 Reactions.....	58
A1.2 Solutions .....	58
A1.3 References for Appendix I .....	62
Appendix 2: Additional Images.....	65
A2.1 Device images.....	65
A2.2 System images .....	66
A2.3 Assorted microplasma images .....	67
Distribution .....	70

## FIGURES

Figure 1: SEM images of microplasma devices .....	13
Figure 2: System, circuit and device schematics .....	15
Figure 3: Electric field determined by the global model .....	17
Figure 4: Device current, voltage and optical output for nanosecond pulsing .....	18
Figure 5: CCD images in the visible spectrum .....	18
Figure 6: Optical scans of specific emission lines as a function of pulse width. ....	21
Figure 7: Nitrogen energy levels .....	22
Figure 8: Integrated emissions from lines of interest as a function of pulse width. ....	25
Figure 9: Test system modification for RF operation.....	31
Figure 10: Example of voltage with time for RF pulsing.....	32
Figure 11: RF operation.....	33
Figure 12: Optical images under RF driving .....	34
Figure 13: Suppression of UV by RF pulsing. ....	34
Figure 14: SEM cross-section and Ne discharge .....	39
Figure 15: 20-degree 3D sector model used for simulations.....	40
Figure 16: Mesh used for all simulations .....	41
Figure 17: Cross sections for kinetic interactions used in the model .....	43
Figure 18: Progression of number densities for e-, Ne+, and Ne(1s <sub>2,4</sub> ) for $V = 250$ V drive voltage.....	48
Figure 19: Comparison of excited state densities at $t = 200$ ns for $V = 250$ V drive voltage.....	48
Figure 20: Initial $t = 0$ ns and final $t = 200$ ns potentials and fields for $V = 250$ V drive voltage.....	49
Figure 21: Time histories of currents and anode potentials for each of the simulated voltages....	51
Figure 22: Velocity distribution functions for e- (left) and Ne+ (right) for three regions, as marked on the e- density plot.....	52
Figure 23: Electric field applied for the simulations of 160 ns pulselwidth.....	60
Figure 24: Electron temperature for a 160 ns pulselwidth simulation .....	60
Figure 25: The evolution of the electron and neon species densities of the 160 ns pulse. ....	61
Figure 26: Emission dynamics determined by the global model for the 160 ns pulse width.....	62

## TABLES

Table 1: Physical parameters of the discharge system. ....	39
Table 2: Interactions included in the simulations .....	42
Table 3: Reaction rates used in the Global Model.....	59

## NOMENCLATURE

MD	Microplasma Device
UV	Ultraviolet Light
VUV	Vacuum Ultraviolet
DC	Direct Current
RF	Radio Frequency
PIC-MC	Particle-In-Cell Monte Carlo
DSMC	Direct Simulation Monte Carlo
DOE	Department of Energy
SNL	Sandia National Laboratories



## 1. INTRODUCTION

This project investigated several fundamental aspects of Microplasma Devices (MD), their scaling into the microdomain, and their UV emission physics. The physics of scaling allows MD to operate near atmospheric pressure where enhanced collision dynamics efficiently create excimers. These produce deep ultraviolet (UV) emissions as short as 65 nm. Laser emissions, in contrast, fall off strongly below 200 nm due to a lack of transparency in solid materials in this regime. Thus, MD light sources are attractive for deep UV applications such as in chemical photo-ionization and atomic or quantum physics. As an example, an efficient light source at 163 nm would provide a direct means of probing atomic clock transitions in a  $^{27}\text{Al}$  atomic clock. It is important to emphasize that in many applications it would be useful to have a tunable UV source. In the case of chemical detection, the ability to adjust the ionization potential of a photo-ionization source in real time would permit one to selectively ionize only those species in a mixture with ionization potentials lower than the source.

This LDRD explored two hypotheses. First, that MD spectral emission can be modified real time by real-time manipulation of plasma voltage bias or current driving conditions. Second, MDs are useful light sources for applications below 200 nm where laser emissions diminish. The first hypothesis was verified using a McPherson 225 VUV spectrometer and pulse capture techniques to inspect emission from a custom MD built in Sandia National Laboratories' MESA clean room. We demonstrated that long wavelength plasma emission lines diminish more rapidly than deep UV lines with decreasing pulse width. RF operation suppresses UV emissions even further relative to pulsed operation. This means that by switching from DC to pulsed mode, or better yet for device lifetime, pulsed to RF operation, we can restrict deep UV emissions. This then allows for on-the-fly tuning of the ionization energy of a microplasma photo-ionization source. We also showed the ability to create transitions in impurity molecules in the MD environment down to 120 nm, supporting the second hypothesis.

This work impacts the fundamental science and engineering of plasmas and in particular the relatively new field of microplasmas. It also impacts many missions of Sandia National Laboratory including those related to nuclear weapons, national and homeland security, defense systems, global security and energy and climate by enabling new detector concepts based on microplasma devices.



## 2. SPECTRA OF NANOSECOND PULSED MD IN NEON

Portable applications of microplasma discharges mandate operation in the presence of contaminant species. This paper examines the temporal evolution of microdischarge optical and ultraviolet emissions during pulsed operation by experimental methods. By varying the pulse length of a microdischarge initiated in a 4-hole silicon microcavity array operating in a 655 Torr ambient primarily composed of Ne, we were able to measure the emission growth rates for different contaminant species native to the discharge environment as a function of pulse length. It was found that emission from hydrogen and oxygen impurities demonstrated similar rates of change, while emissions from molecular and atomic nitrogen, measured at 337.1 and 120 nm's respectively, exhibited the lowest rate of change. We conclude that it is likely that O<sub>2</sub> undergoes the same resonant energy transfer process between rare gas excimers that has been shown for H<sub>2</sub>. Further, efficient resonant processes were found to be favored during ignition and extinction phases of the pulse, while emission at the 337.1 nm line from N<sub>2</sub> was favored during the intermediate stage of the plasma. In addition to experimental results, a zero-dimensional analysis is also presented to further understand the nature of the microdischarge.

### 2.1. Introduction

Microhollow cathode discharges (MHCD) have been shown to be an efficient tool for the generation of vacuum ultraviolet (VUV) emissions via resonant energy transfer between rare gas excimers and trace gases at atmospheric pressures [1] [2] [3]. MHCDs consist of an arbitrarily shaped metallic anode and a cylindrical hollow cathode open on at least one side. Despite the name, many differences exist between traditional hollow cathode discharges and MHCDs. First and foremost, MHCDs have three modes of operation – at low currents an abnormal glow is present, which transitions to self-pulsed and normal mode as current is increased.

As a three-body process, excimer generation requires a high collision frequency between particles of sufficient energy to facilitate the reaction. These constraints require high gas density, on the order of atmospheric pressure, and high particle energies, 16 eV or greater in the case of Ne. Hollow cathode discharges feature a non-Maxwellian energy distribution with highly energetic pendulum electrons [4] and beam electrons contributing a significant fraction to the total [5], which makes them a reasonable choice to facilitate excimer formation.

The range of operating pressures available to MHCD devices varies inversely with the hollow cathode diameter according to the Allis-White similarity law [6]. This limits the device dimensions under high pressure conditions on the order of  $p \cdot D = 0.1\text{-}10 \text{ Torr} \cdot \text{cm}$  depending on gas and electrode material. In 1996 Schoenbach et al demonstrated the initiation of a microhollow cathode discharge with a diameter of 75  $\mu\text{m}$  in pressures up to 350 Torr. Further work has since been reported plasma generation at atmospheric pressures in silicon microcavities with diameters on the order of 100  $\mu\text{m}$  [7] [8] [9] [10].

Previous work has reported driving MHCD devices in DC [10, 11], pulsed [12] and RF [13] conditions. Where DC operation allows the plasma to reach a state of steady optical emissions and current flow, pulsed and RF modes favor transient states that allow for much higher energy electrons due to pulsed electron heating [14].

As the field of MHCD science continues to grow, field-deployable devices become a possibility. A major challenge to this progression becomes gas contamination from the environment. Even trace amounts of impurities can significantly impact the spectral output of a device. As gas impurities will be nearly impossible to eliminate in the near term, the present correspondence seeks to explore the relative trends exhibited by the common contaminants N<sub>2</sub>, H<sub>2</sub>, and O<sub>2</sub>, under ns-pulsed conditions in near-atmospheric pressure neon. To further explore the underlying physics responsible for experimental phenomena, a zero-dimensional (0-D) model has also been developed, which attempts to mimic experimental conditions.

## 2.1. Microplasma device array fabrication testing and failure analysis

### 2.1.1 Fabrication

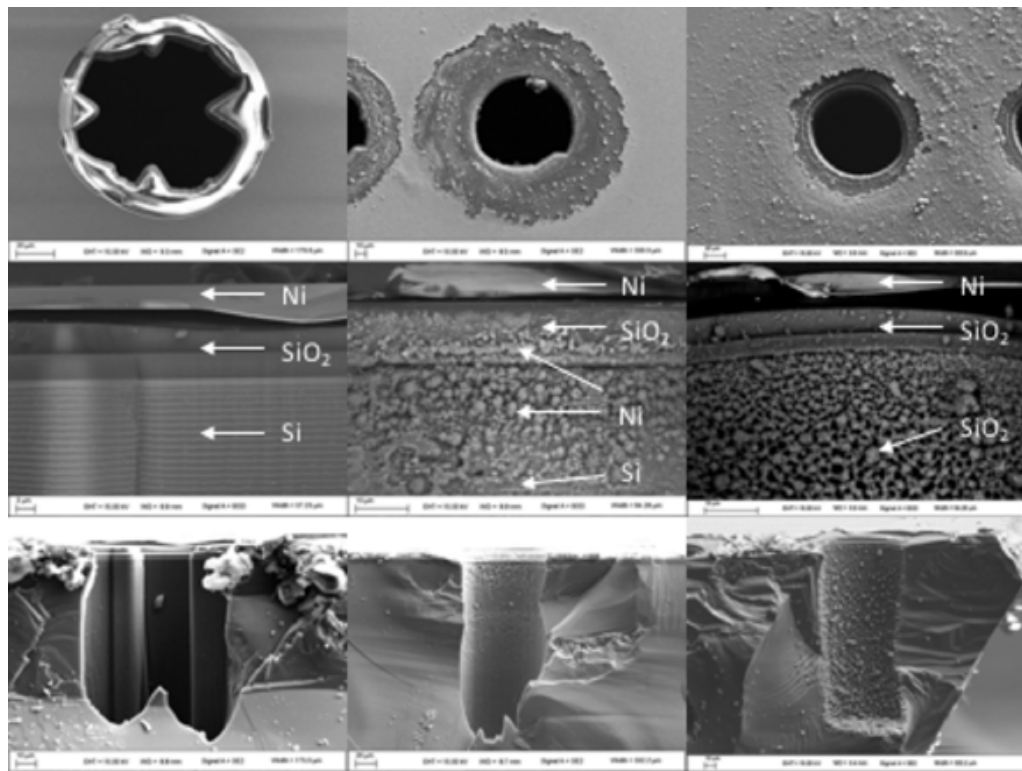
The 4-cavity microdischarge array used in these experiments was constructed in 685  $\mu\text{m}$  thick p-type silicon (2-20  $\Omega\text{ cm}$ ). To create an insulating layer between a top electrode and the doped silicon, thermal steam oxidation was used to grow a 3  $\mu\text{m}$  silicon dioxide, which was followed by the growth of a 7  $\mu\text{m}$  PECVD (plasma enhanced chemical vapor deposition) silicon oxide layer. The oxide was then patterned by optical photolithography and etched using Plasmatherm inductively coupled plasma (ICP) etcher. To form the top electrode a 200  $\text{\AA}$  titanium adhesion layer followed by a 1  $\mu\text{m}$  Nickel layer were applied via evaporation. The total surface area of the top electrode was 4  $\text{mm}^2$ . Four cavities arranged in a 200  $\mu\text{m}$  center-to-center square, 100  $\mu\text{m}$  in diameter and 200  $\mu\text{m}$  deep, were formed by a BOSCH deep reactive-ion etching (DRIE) process. The thermal silicon dioxide on the rear surface was then stripped using a buffered oxide etch (BOE) while the top surface was protected with photoresist. Next, an aluminum electrode was evaporated onto the rear wafer surface, which served as an electrical ground electrode. The silicon chips were then affixed to a custom ceramic circuit board using a conductive epoxy and the top electrode was wire-bonded to an electrode pad on the circuit board. Finally, to avoid arcing, non-conductive epoxy was applied to the edges of the silicon chip and degassed for 1-2 hours in a vacuum oven set to 50  $^{\circ}\text{C}$  and evacuated to  $\sim$ 10 Torr.

### 2.1.2 Testing in DC and Pulsed Modes

Figure 1 shows images from a scanning electron microscope (SEM) of a device before (Figure 1(a-c)) and after use in DC (Figure 1(d-f)) and ns pulsed (Figure 1(g-i)) modes. As can be seen in figure 1(a-b), prior to use, both the top electrode and the cavity surface are smooth and well defined. Analysis with energy dispersive spectroscopy (EDS) confirms the chemical make-up of the device as, from top to bottom, nickel, silicon oxide, and silicon. DC operation of microdischarge devices has been extensively covered [15] [11] [16] [17] so this paper will only discuss differences in device lifespan and failure mode between ns-pulsed and DC modes. In Figures 1(d-f) the device was used in DC mode until it would pass current in the absence of plasma (shorting), which is defined here as device failure. Note the extensive regression of the top nickel electrode, which is now  $> 40 \mu\text{m}$  from the cavity. Also notice the sputtering of nickel over the top surface and into the hole. In this case, EDS confirms the presence of nickel extending from the top layer, across the oxide and down into the silicon dielectric, which may lead to a short circuit between the electrodes as observed by Kulsreshath *et al* [17]. However, the specific short circuit path from the electrode into the cavity could not be determined from

these images. Attempts are being made to build a top electrode that is more resistant to sputtering in order to extend device life.

Pulsed operation showed multiple advantages over a DC discharge. By substantially reducing the time that the plasma was present and that current was flowing, damage to the device due to thermalization of the device walls and electrodes was avoided. Figure 1(h) shows that the top electrode only receded  $\sim 10 \mu\text{m}$ , much less than in DC. EDS confirms the absence of even trace amounts of nickel in either the cavity or crossing the top oxide layer. This further supports the idea that by operating in pulsed mode, thermalization of the metal electrode is reduced. On the other hand, a high concentration of oxygen is present throughout the pulsed discharge cavity. Further, when operated in ns-pulsed mode, the devices would not catastrophically fail as in DC. Current would drop and multiple ignition spikes would form over the course of a single pulse. This behavior could be reduced by increasing the driving voltage. A possible explanation is that during ns-pulsed mode oxygen reacted with the doped silicon, creating a porous insulating silicon dioxide structure on the surface of the cavity. As will be discussed later, it is likely that this increased amount of oxygen in the pulsed discharge cavity caused an increase in the oxygen content within the plasma gas mixture, and a similar increase in emission of the 130.2 nm oxygen line.



The left column shows three views of an unused MHCD from the top, cross section (close up of the electrode region) and complete cross-section view. The central column has the same three views after use in DC operation to failure. The right column has the views after nanosecond pulsed mode until failure.

**Figure 1: SEM images of microplasma devices.**

## 2.2. Experimental Apparatus

Figure 2 shows the schematic of the device, circuitry, and surrounding equipment. Experiments were conducted in a  $\sim 1$  L vacuum chamber capable of sustaining pressures in a range of  $10^{-6}$  to  $10^3$  Torr. Following evacuation with a turbomolecular vacuum pump and after the chamber was sealed off from the vacuum, the chamber pressure would immediately rise from  $\sim 10^{-5}$  to  $\sim 10^{-3}$  Torr, presumably due to off-gassing of the epoxy, other plastics in the chamber, and the steel chamber itself. It is assumed that this was the main contributor to gas impurities seen in the following experiments, and representative of impurities that will be seen by microdischarges in practical use. The chamber was then back-filled with the desired gas. The pressure was measured by a Pfeiffer CMR-361 pressure gauge (0.1 Torr – 825 Torr) and a Varian FRG-700 vacuum gauge ( $4 \times 10^{-9}$  Torr – 1 Torr).

Two view ports were installed on the chamber to view the plasma. The first, made of Kodial glass, faced up for direct viewing. The second, made of  $\text{MgF}_2$ , faced into a McPherson 225 one-meter vacuum spectrometer that was equipped with a 600 line/mm grating capable of  $0.3 \text{ \AA}$  resolution. The spectrometer cavity was maintained at  $10^{-6}$  Torr with another turbomolecular vacuum pump. The detection end of the spectrometer had a window coated with a sodium salicylate scintillating layer. Next, a Hamamatsu R6095 photomultiplier tube powered at 800 V was used to detect optical emissions. The PMT signal was amplified with a Stanford Research SR445A and acquired with a Stanford Research SR430 scaler.

A DC power supply (2500V/25W) was used to ignite the micro-discharges. Relative concentrations of chemical species in the chamber were determined with a SRS RGA 100 that was connected to the chamber vacuum line. A leak valve was used to bleed gas into the differentially pumped vacuum line for analysis.

In pulsed mode, the circuit was reconfigured to allow the plasma to turn on quickly. A  $100 \text{ k}\Omega$  resistor followed by a  $1 \text{ nF}$  capacitor were placed between the power supply and a DVI PVX-4150 pulse generator to control the load on the power supply. An Agilent 33210A function generator was used to produce a square wave pulse that initiated the pulse generator. The current was measured before and after the device using inductive current probes. A  $5\text{kV}$  voltage probe was connected directly to the bare wire before the first current probe. A  $1 \text{ k}\Omega$  resistance was placed between the last current probe and ground to serve as a ballast resistor. The voltage and current were both recorded using a Tektronix MSO 5104B oscilloscope terminated at  $1 \text{ M}\Omega$  and  $50 \Omega$  respectively.

This work focuses on pulsed operation with limited reference to DC operation. For reference, Figure 2 describes both circuits. In both the DC and the pulsed experiments the device was oriented with the top metal as the anode (biased positive) and the silicon cavity as the cathode at ground.

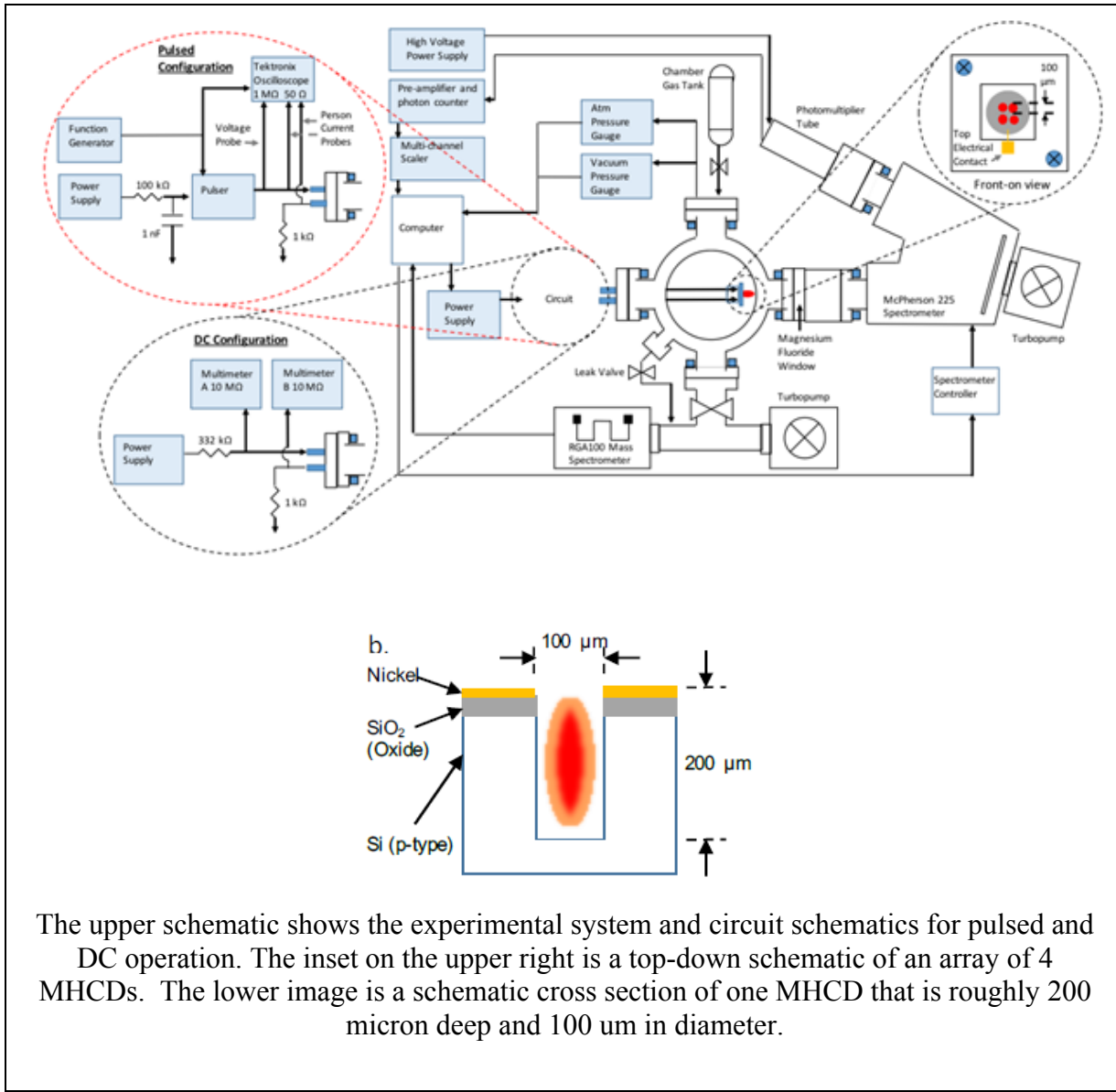


**Figure 2: System, circuit and device schematics.**

## 2.3 Global Model

A zero-dimensional model was created to investigate the possible processes occurring in the MHCD system. A global model is a zero-dimensional model of a plasma which assumes spatial homogeneity. While it cannot capture the full complexity of a real plasma, it is suitable for basic characterization of the plasma chemistry dynamics. A detailed explanation of the model as well as a complete list of results will be the subject of a future publication. Also, a table of the specific reactions that were included in the model is provided in the appendix.

Briefly, most global models involve two governing equations, one for the number densities of the atomic and molecular species, and another to follow the evolution of the electron energy in the system. The former can be generally expressed as:

$$\frac{dn}{dt} = G - L$$

where  $n$  represents the density for some species of interest,  $G$  is the rate at which the species is produced, and  $L$  is the rate at which the species is lost. Gain and loss mechanisms vary greatly depending on the system in question and may represent excitation, ionization, detachment, or spontaneous emission among many other processes. The gain or loss terms may also represent physical processes that are not related to particle-particle interactions. One such example is the outflux of particles from the system. Despite the assumption of a zero-dimensional system, the microdischarge has boundaries which result in the outflux of particles from the region of concern. We describe this with a simple model based on the Bohm flux [18] at a surface, taking the positive ion flux to be equal to  $0.6In_iAc_s$ , where  $n_i$  is the ion density,  $A$  is the characteristic collection area, and  $c_s$  is the Bohm velocity for the ion in question. The collection area is assumed to be the internal area of the microdischarge geometry. Additionally, we ignore complications in the Bohm criterion related to the presence of multiple ion species [19]. Finally, we assume that the outflux of electrons is equal to the total outflux of ions.

The dynamics of the electron energy are considered using the equation,

$$\frac{dT_e}{dt} = \frac{2}{3k_B n_e} \left[ \frac{e^2 n_e E(t)}{m_e K_m n_g} - 3n_e K_m n_g \frac{m_e}{m_g} \frac{3}{2} k_B (T_e - T_g) - \sum \Delta \epsilon \right]$$

Here,  $T_e$  is the electron temperature,  $k_B$  is Boltzmann's constant,  $n_e$  is the electron density,  $E$  is the (time-dependent) applied electric field,  $K_m$  is the (temperature-dependent) momentum transfer rate,  $n_g$  is the neutral gas density,  $T_g$  is the gas temperature, and  $\Delta \epsilon$  is the energy change as the result of some reaction. The three terms in this equation represent the electron energy gained by the field, the energy loss due to neutral collisions, and the energy gained (or lost) due to reactions involving electrons.

The applied electric field shape (Figure 3) was chosen to be consistent with the observed emission dynamics as described in the section 2.4.3 Optical Traces.

The electron energy distribution was assumed to be Maxwellian. It is probable that this assumption is not accurate during the initiation of the microdischarge given the large reduced electric fields. This will most likely result in an underestimate of the excitation rates for higher levels. Future simulations could address this by including a bimodal electron energy distribution as described by Badareu and Popescu [20].

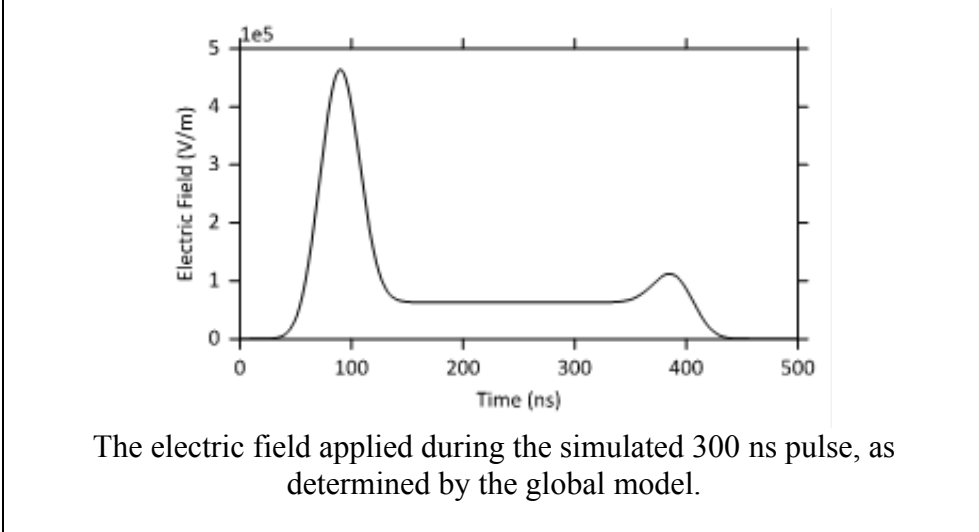


**Figure 3: Electric field determined by the global model.**

## 2.4 Results

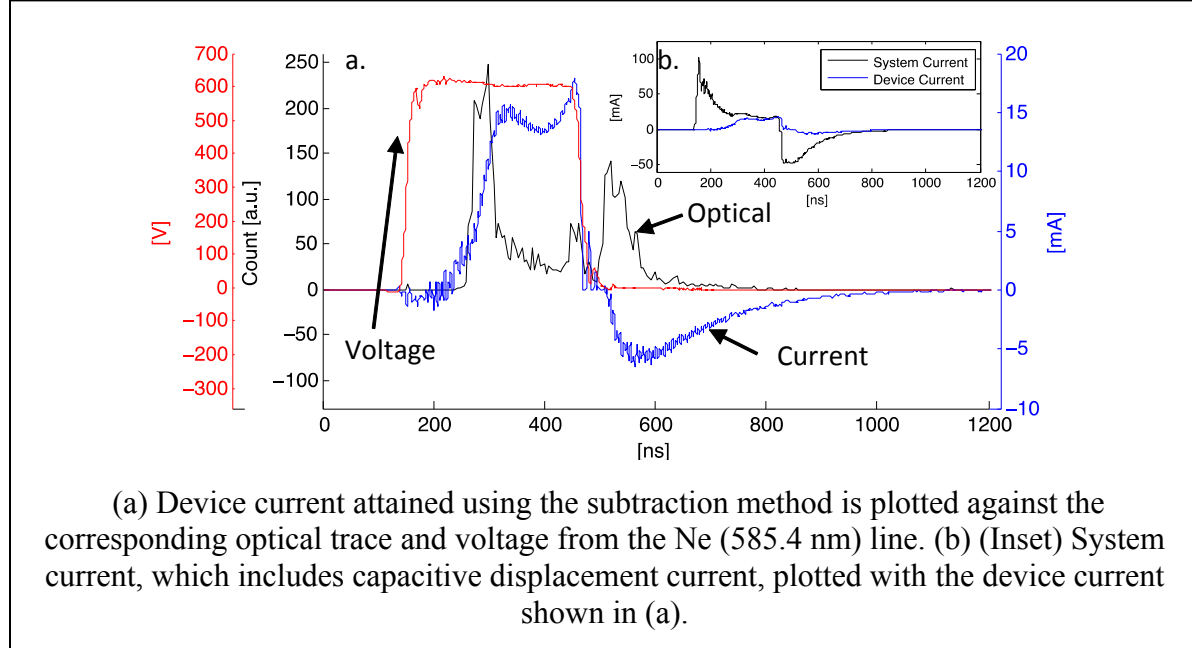
### 2.4.1 Electrical Characteristics

Figure 4 shows the current, voltage and optical traces during ns pulsed operation. The device current, shown in figure 4(a-b), was measured and calculated using a subtractive method where the baseline displacement current due to capacitance within the system was measured by applying the standard pulsed driving voltage to the device while the device chamber was evacuated to  $\sim 10^{-5}$  Torr, a procedure which precluded the formation of a plasma. The dark current under these conditions was calculated to be on the order of one  $\mu$ A, which was 5 orders of magnitude below the nominal operating current. The system current was then measured during discharge operation. The baseline current was then subtracted from the active system current to give the device current.

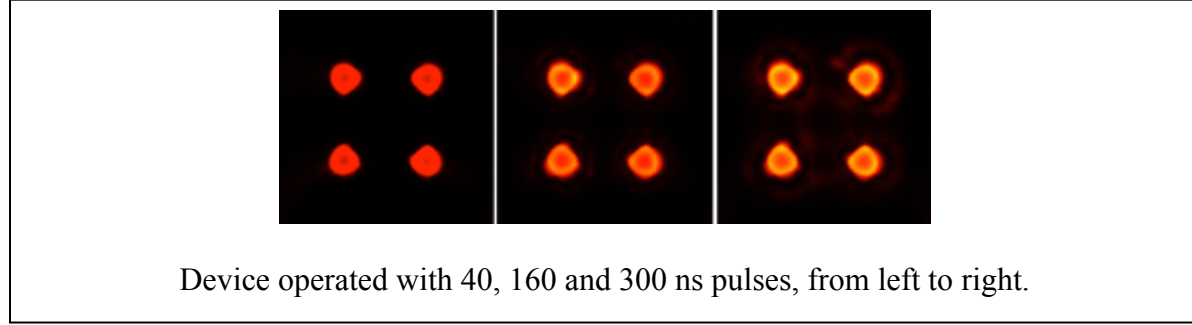
Figure 4(a) shows the temporally resolved optical signal measured at 585.3 nm, the device current and voltage traces over the span of a 300 ns pulse. By comparing the discharge current to the system current in Figure 4(b), one can see the non-trivial displacement current present during the initiation and extinction of the pulse. While the system displacement current peaked during the initiation and extinction phases of the pulse, the actual device current reached its maximum during the standard phase between ignition and extinction. Gamez *et al.* [21] found that the electron temperature was highest during the ignition (pre-optical peak) of a neon plasma. They also found that the converse was true for electron density, which was low during pre-ignition and then increased over the course of the pulse. This corresponds with a higher optical output during the transient stages, but a higher current in the middle stages as seen in figure 4(a).

Figure 5 shows visible emissions during operation in pulsed mode at pulse widths of 40, 160, and 300 ns. Note the near uniform character of the plasma with respect to single cavities as well as the uniformity when comparing cavities to each other. The operating conditions during these experiments were within the bounds of an abnormal discharge (6.55 Torr cm) with an increase in

the highly energetic tail of the electron energy distribution [8], which allows for increased creation of high energy states such as the neon excimer.



**Figure 4: Device current, voltage and optical output for nanosecond pulsing.**



**Figure 5: CCD images in the visible spectrum.**

Under conditions where the voltage rise time ( $t_V$ ) is much faster than the characteristic time for kinetic energy transfer between electrons and the neutral gas atoms ( $\tau_e$ ), electrons reach higher energies in the transient stages of the plasma than during standard operation [22]. In our case, the measured voltage rise time (10-90% of peak voltage) was 21.5 ns. Bolouki *et al* [23] used Thompson electron scattering under conditions similar to those presented in this paper to determine an electron temperature of  $\sim 2.5$  eV at 15 ns after initiation of the plasma, which leads to a  $\tau_e = 10^6$  ns [22]. Our system is thought to have an electron temperature closer to 4.5 eV ( $\tau_e = 10^4$  ns) based on simulation, which will be discussed later. During discharge initiation, space charge is negligible and electrons in the system are exposed to the full electric field. Electron densities are small, but their mean energy is likely higher (or comparable to) the reaction energy thresholds that will be discussed later. After initiation, space charge becomes important and

likely pushes most of the potential drop to a small sheath region. Thus, a large portion of the plasma becomes relatively field free, resulting in a drop in electron temperature.

#### 2.4.2 Chamber Gas

A differentially pumped SRS RGA100 was used to determine relative concentrations of gas species based on their partial pressures. The highest concentration contaminants present in the discharge chamber were N<sub>2</sub> (0.17%), H<sub>2</sub> (0.14%), H<sub>2</sub>O (0.04%), and O<sub>2</sub> (0.04%), with neon comprising the balance. The reported values were acquired by first subtracting the baseline from the chamber RGA signal, then correcting for the RGA's relative sensitivity using the manufacturer's published values.

#### 2.4.3 Optical Traces

Presented here are the results from the MHCD device in pulsed mode. The device was pulsed in the range of 40-300 ns at 10 kHz with a power supply biased to +950 V. Due to the internal resistance of the pulser, the voltage applied to the device was approximately +630 V as measured from the voltage probe. The chamber was backfilled to 655 Torr with Ne. To eliminate arcing between the device wires and the vacuum chamber, fish-spine ceramic insulators were installed on the wires between the chamber electrical feedthroughs and the device. As the RGA results showed, the plasma gas primarily contained the species Ne, H, O, N and N<sub>2</sub>.

For the following analysis, representative lines were chosen for each species to examine the temporal character of their emissions. The 120.0, 121.6, 130.2, 337.1 and 585.3 nm lines correspond to N (I), H (I), O (I), N<sub>2</sub> (I) and Ne (I) respectively.

Figure 6 shows the optical traces from the individual emission lines over different pulse widths normalized by dividing by each species maximum value. Each trace is the average of three scans conducted in a random order. In each panel, the 585.3 nm Ne line is plotted in grey to give a frame of reference for each species. This line results from the transition from the 2s<sup>2</sup>2p<sup>3</sup>(<sup>4</sup>S<sup>o</sup>)3s<sup>3</sup>S<sup>o</sup> 1 state down to 2s<sup>2</sup>2p<sup>4</sup>3P 1 state [24].

The emission pulse can be broken into three parts, which were exhibited by each species investigated here. Briefly, as shown in Figure 6(d), the emissions are observed to peak soon after the pulse is applied, which we term, ignition. This is followed by a decline in emission termed the intermediate stage. As the pulse ends and the applied voltage goes to zero, we witness a second ignition spike corresponding with a spike in displacement current, which we call, extinction. The ignition peak is believed to be caused by high fields in the bulk of the device prior to the formation of significant space charge. As the plasma density increases to the point where it can shield out the applied field, much of the potential drop is removed to the boundary of the plasma, thus reducing the field experienced by the bulk of the plasma. In the 40 ns pulse regime the ignition and extinction phases were compressed together and the intermediate phase was not observed.

In each pulse length, the ignition and extinction peaks from the Ne line preceded that of the contaminant species by 20-40 ns. The Ne emission then dropped dramatically as the other

species ignited and finally settled at a semi-stable output as seen in the intermediate portion of pulses  $> 90$  ns.

In this study, the 337 nm line was focused on to investigate emissions from the second positive band of N<sub>2</sub> (figure 6(d)). Following the emission of the Ne line, molecular nitrogen was the next to emit. The primary N<sub>2</sub> (I) line at 337.1 nm followed Ne's first peak by  $12 \pm 5$  ns. During the intermediate phase, where the Ne line showed a flat output, the N<sub>2</sub> (I) line showed a period of sustained linear growth in intensity. It is likely that, following the initial transition responsible for the 337.1 nm line ( $C^3\Pi_u \rightarrow B^3\Pi_g$ ), the nitrogen molecule achieved a metastable state [25] by degrading through the first positive system  $B^3\Pi_g \rightarrow A^3\Sigma_u^+$  [26]. As the metastable state,  $A^3\Sigma_u^+$  is at 5.169 eV [27], the nitrogen electron in this arrangement requires only 5.86 eV to be promoted back to  $C^3\Pi_u$  (figure 7), substantially lowering the energy barrier for emission of the 337.1 nm line. Also, both pathways  $A^3\Sigma_u^+ \rightarrow C^3\Pi_u$  and  $X^1\Sigma_g^+ \rightarrow C^3\Pi_u$  can be accomplished in a single step, while the excitation of H and O requires dissociation and excitation, which can be accomplished in one step, but only at energies  $> \sim 15$  eV.

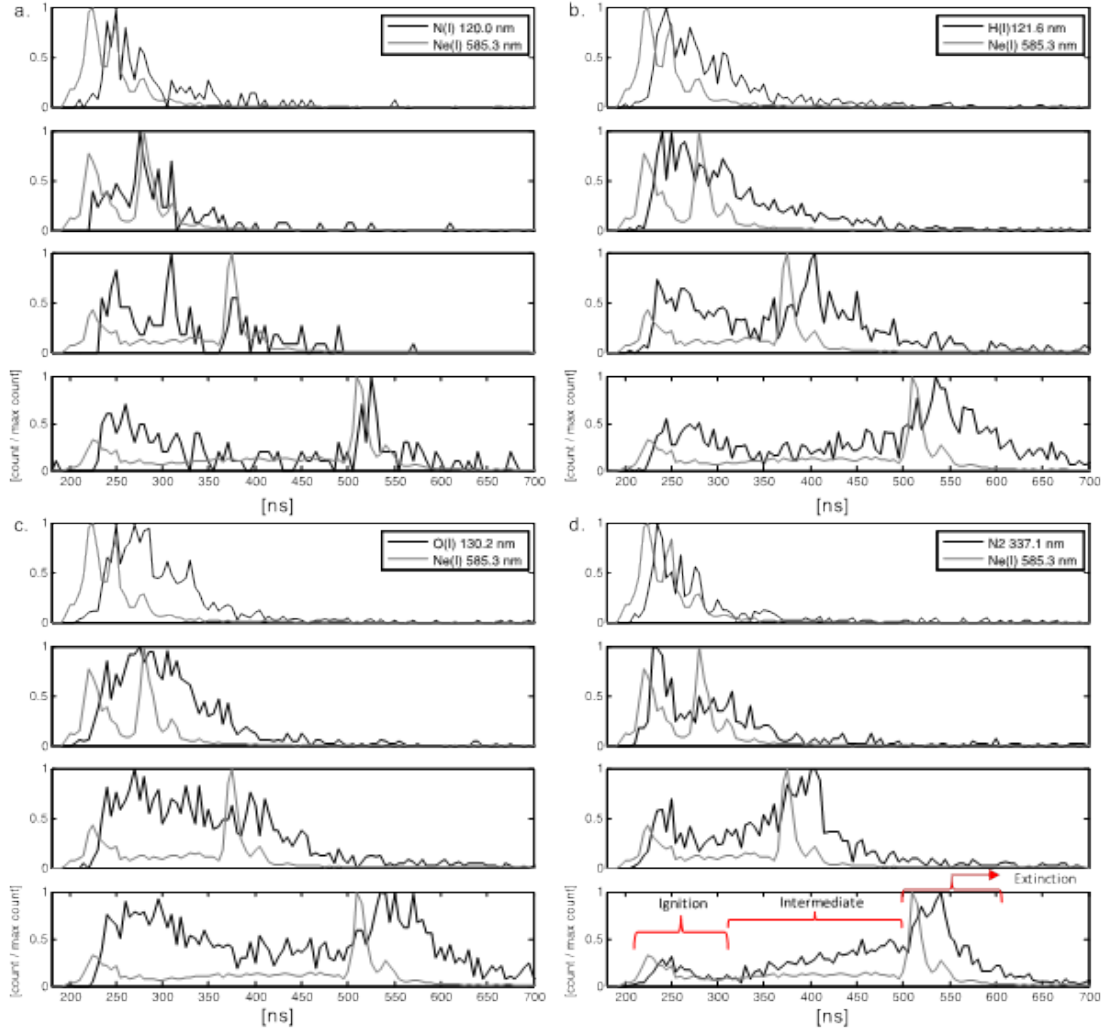
The study of atomic oxygen was carried out by focusing on the 130.2 nm line of O (I) (Figure 6(c)), which is part of a tight triplet created by the energy level transition from  $2s^22p^3(^4S^o)3s\ ^3S^o$  1 down to  $2s^22p^4\ ^3P$  1 [24]. While the other species exhibited an ignition ‘spike’ lasting 25-50 ns, the O (I) line displayed an ignition ‘plateau’ that persisted on the order of 100 ns with a slower rate of decay than the other species during the intermediate stage, suggesting that non-trivial emission trapping could be present, likely due to an increased oxygen concentration within the plasma. This behavior is also exhibited after the extinction spike.

The Lyman- $\alpha$  line of Hydrogen at 121.6 nm (Figure 6(b)) mirrors the behavior of the Ne line, but with a similar delay to that of N (I). It peaked following Ne by  $17 \pm 4$  ns. Like the N<sub>2</sub> (I) line, the H (I) line also exhibited a positive slope over the intermediate period during the 300 ns pulse, suggesting that an excitation source of sufficient energy, either electrons or Ne excimers, were still present in the intermediate stage.

The excited N (I) line at 120.0 nm, resulting from the transition between  $2s^22p^2(^3P)3s\ ^4P$  1/2 down to  $2s^22p^3\ ^4S^o$  3/2 [24], was the last to show peak emission, reaching its first maximum  $20 \pm 9$  ns after the first maximum of the Ne (I) line. Emission from N (I) first requires the dissociation of N<sub>2</sub> with a much higher dissociation energy (9.75 eV) than H<sub>2</sub> or O<sub>2</sub>. Further, while the total dissociation and excitation energy required for the N (I) line is roughly the same as the excitation energy for the Ne line, excitation for Ne is a single step process and Ne is present at a much greater concentration. Further, while excitation of the Ne 120.0 nm line requires roughly the same energy as the Ne line at 585.3 nm ( $\sim 20$  eV), the concentration of Ne is  $> 3$  orders of magnitude greater than N.

It is important to note that emissions from H (I), O (I), and N (I) are all ground state transitions and are thus subject to emission trapping. However, without a clear understanding of the concentrations of each species it was not possible under specific time constraints to conduct a detailed analysis of this issue. With concentrations  $< 0.2\%$ , and a 200  $\mu\text{m}$  thick plasma with an pulse time that accounted  $\leq 0.3\%$  of the operational time, it may be reasonable to assume that

trapping is negligible for most species, but further analysis is required to achieve a high level of confidence.



The pulses shown are 40, 90, 160, and 300 ns from top to bottom. Each line is set against the optical trace from the Ne line at 585.4 nm as a reference.

**Figure 6: Optical scans of specific emission lines as a function of pulse width.**

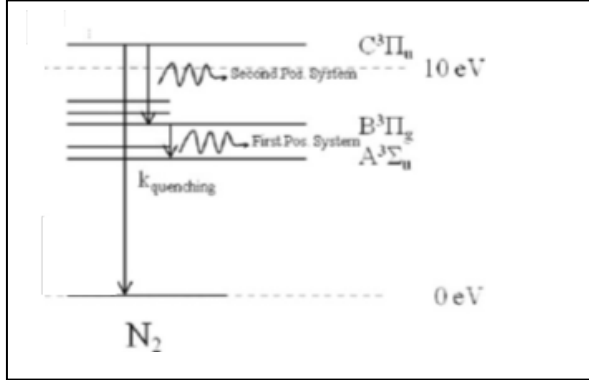


**Figure 7: Nitrogen energy levels.**

#### 2.4.4 Integrated Emissions

Figure 8 shows the line-specific optical output as a function of pulse width integrated over each pulse from both the experiment (Figure 8(a)) and the model (Figure 8(b & c)). The data has been normalized by subtracting the lowest value of each species then dividing by the maximum value of the 585.3 nm line in order to focus on the relative behavior of each species. The values reported in Figure 8(a) were corrected via a calibration transfer function. The transfer function was created by obtaining a spectrum from a 632 McPherson deuterium lamp with our spectrometer system, which was then divided by calibrated spectra provided by McPherson. Though the specific lamp used here was not calibrated, the provided spectra were found to vary over the sample space by < 10 %. As a result, we assume our final values contain at least that level of uncertainty. The calibrated PMT data were then divided by the energy associated with each line to yield a relative photon count, which is a comparable value, both between lines and between experiment and model.

Figure 8(b) shows the results from the model using the gas concentrations that were measured during the experiment. As can be seen when comparing figure 8(a) and (b), the model predicts a far lower emission from the oxygen line than was witnessed experimentally. As mentioned in the section, *Description of array (fabrication and failure)*, it was determined to be likely that a higher concentration of oxygen existed in the chamber than was measured. This is likely due to oxygen reacting with the silicon in the cavity. To produce figure 8(c), the oxygen concentration was increased  $\sim 300\%$  to equal that of hydrogen, which produced an increase in oxygen emissions, though not to the level witnessed experimentally. We present this as further evidence that the oxygen within the chamber was higher than was measured in the bulk chamber gas. Secondly, as the oxygen emissions increased, the hydrogen emissions decreased. We hypothesize that it is likely that oxygen and hydrogen share at least one similar excitation pathway.

Wieser *et al* [1] demonstrated that resonant energy transfer between neon excimers and hydrogen (eq. 1 & 2) contaminants was a possible excitation source for the Lyman- $\alpha$  line at 121.6 nm. Kurunczi *et al* [2] further characterized the reaction pathway by demonstrating an inverse relationship between the intensity of the Lyman- $\alpha$  line and the 1<sup>st</sup> and 2<sup>nd</sup> continuum of the Ne excimer band as a function of the relative concentrations of H and Ne.



While the densities of the species of interest (O and H) were predicted by the model to be on the order of  $\sim 10^{21} - 10^{22} \text{ m}^{-3}$ , the model also showed a non-trivial Ne excimer density of  $10^{19} \text{ particles m}^{-3}$ . Further, as discussed previously, it is likely that the electron energy distribution features a larger potential for high energy electrons due to a non-thermal distribution, which would increase the excimer concentration. As a result, it is reasonable to assume that excimers contribute to the plasma reaction pathways.

The transition energy released during the decay of the  $\text{Ne}_2^*$  excimer molecule is  $14.8 \pm 0.8 \text{ eV}$ , which compares favorably with the sum of the dissociation and excitation energies of  $\text{H}_2$  (14.68 eV) [28] that are responsible for the Lyman- $\alpha$  line. Compare this to the the dissociation and excitation energies for  $\text{O}_2$ , which sum to 14.67 eV to achieve the state  $2\text{p}3(4\text{S}^*)3\text{s}.3\text{S}^*.1$ , which produces the 130.2 nm line presented in this paper. Due to the similar total energy relating to the oxygen process (eq. 3 & 4), it is possible that the same resonant process occurs and could help explain the shifted emissions seen between H (I) and O (I) in figure 8(b & c). Moselhy *et al* speculated that the resonant process was present between argon and oxygen under similar conditions [3].

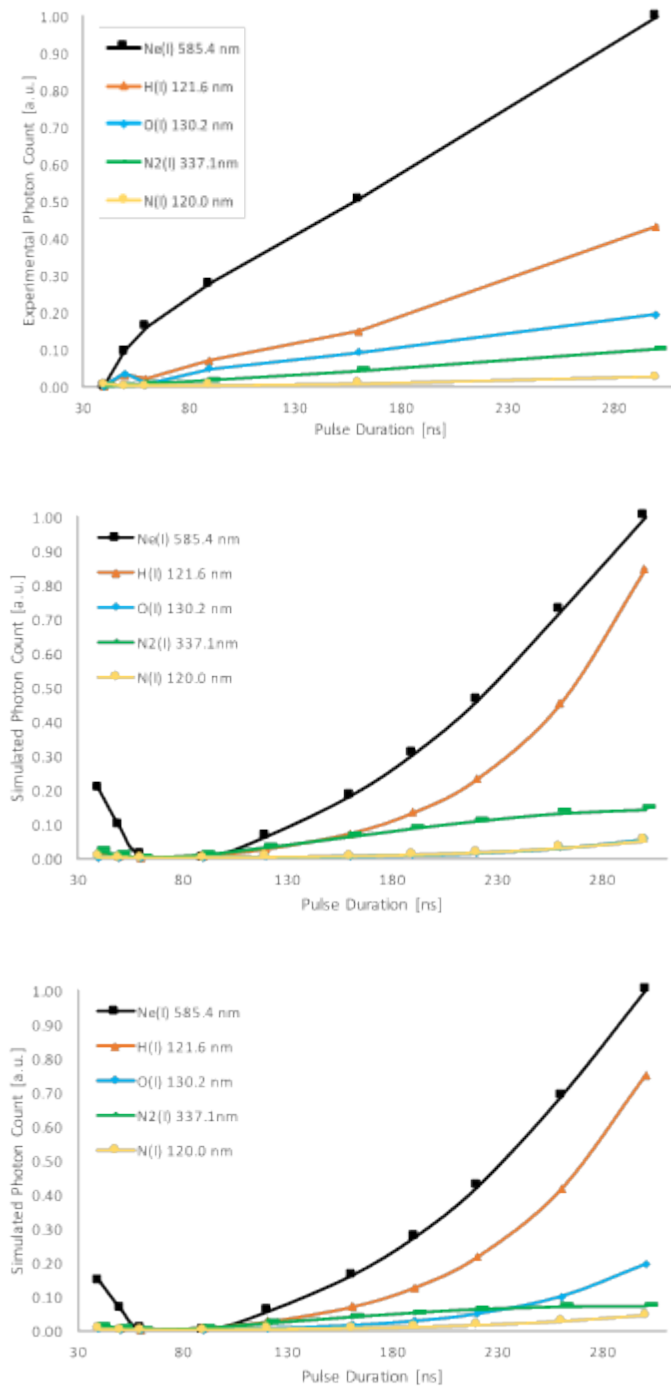


On the other hand, the integrated emissions from the N (I) line at 120.0 nm stayed nearly constant between pulse widths of 40 to 300 ns both experimentally and in both modeled conditions. Nitrogen, with a dissociation energy of 9.75 eV, has no such resonant pathway for excitation of the observed state. As this feature has the highest energy barrier, it is likely that the 120.0 nm line is excited primarily during the ignition and extinction phases of the pulse when a greater concentration of high energy electrons is present. As seen in figure 6, atomic nitrogen emission is detected primarily during the transient ignition and extinction spikes.

Several additional radiative transitions are tracked by the model as detailed in the reactions table (Appendix A). In Figures 8(b) and (c) the transitions plotted are those for which experimental data were available. It should be noted that the radiative transition rates used were those for *untrapped* emissions. In reality, the VUV emissions are all resonance radiation which should be treated appropriately. However, given the complex geometry and unknown experimental densities of atomic oxygen, hydrogen, and nitrogen in the volume between the discharge and the spectrometer window no accounting was made for this effect. In reality, trapping would be expected to increase the effective lifetime of the trapped states shifting the peaks of these emissions relative to untrapped transitions such as  $\text{Ne}(2\text{p}_1) \rightarrow \text{Ne}(1\text{s}_2)$ .

Another notable difference between the model and experiment is that the model predicts a semi-parabolic trend with emissions peaking at the edges of the sample space. This is most likely due to the way the modeled electric field is treated during pulses  $< 90 \text{ ns}$ . In this regime, the ignition

and extinction pulses (Figure 3) begin to overlap and are summed into one larger peak, producing a higher field during this combined ignition/extinction period. An examination of the experimental displacement current showed that this did not occur and that the ignition and extinction spikes remained separate. Without this feature, it is thought that the model will show a positive slope across the entire sample space as currently seen between the pulse widths of 90-300 ns.



Emissions are normalized to their lowest value. The three plots show (a) the experimental results, (b) the 0-D model run with the measured chamber concentrations, and (c) the 0-D model run with the O<sub>2</sub> concentration increased to equal the measured H<sub>2</sub> concentration.

**Figure 8: Integrated emissions from lines of interest as a function of pulse width.**

## 2.5 Conclusions

In future field-portable devices that utilize microdischarges, certain gas impurities will likely be a constant presence and concern. Here we examined the spectral emissions of common impurities field-portable devices would experience – N<sub>2</sub>, O<sub>2</sub>, and H<sub>2</sub> – to characterize typical features witnessed during ns pulsing. Here we present the first, to this author's knowledge, detailed study of these specific contaminant species and their optical emission characteristics as produced by a ns-pulsed MHCD array in a silicon microcavity array. Together, our experiments and model support the hypothesis that the emissions from species capable of near-resonant energy transfer with Ne excimers are more prominent during the high energy transient stages of a ns-pulsed microdischarge. On the other hand, emission from N<sub>2</sub> shows the highest tendency to increase during the intermediate stage of the plasma. Specifically, the emissions of the examined chemical species varied based on their excitation potentials, and the reactions that utilized resonant energy transfer with Ne excimers (O<sub>2</sub>, H<sub>2</sub>) (eq 1-4) were favored during ignition and extinction, while those that featured metastable states (N<sub>2</sub>:  $A^3\Sigma_u^+ \rightarrow C^3\Pi_u \rightarrow B^3\Pi_g$ ) were favored during the intermediate period. This led to high transient emissions from the 121.6 nm and 130.2 nm lines, while emission from N<sub>2</sub> at 337.1 nm featured a prolonged increase during the intermediate period. Emission at the 120 nm line of N(I), which was the state with the highest energy barrier to excitation, showed very little change in integrated intensity and primarily emitted during the ignition and extinction pulses. The ignition and extinction phases also corresponded with a spike in displacement current produced by the system circuitry.

Also presented is an analysis of the failure modes of the devices when operated in DC vs ns-pulsed mode. It was found that in DC operation, sputtered nickel from the top electrode was visible crossing the insulating oxide layer and that the device would fail by passing current without the ignition of a plasma. Failure for a ns-pulsed device may have followed the growth of an insulating oxide layer around the inside of the doped silicon cavity, which could be alleviated by increasing the applied voltage to retain normal function until the layer became too thick for any current to flow. It is likely this reaction increased the cavity oxygen concentration by a factor of four or greater, which led to substantially increased emissions of the 130.2 nm triplet and was predicted based on measured chamber gas concentrations.

A zero-dimensional model was presented as further evidence for the specific reactions that are thought to be responsible for the relative strength of each line. The comparison between model and experiment demonstrated it was likely that the chamber concentration of oxygen was a poor measure of the actual oxygen reacting in the plasma cavity. Further adjustments to the model are underway, such as the inclusion of a non-Maxwellian electron temperature distribution.

## 2.6 References for Section 2

1. Wieser, J., M. Salvermoser, L.H. Shaw, A. Ulrich, D.E. Murnick, and H. Dahi, *Lyman-alpha emission via resonant energy transfer*. *Atomic Molecular Optical Physics*, 1998. **31**: p. 4589-4597.
2. P. Kurunczi, H.S., K. Becker, *Hydrogen Lyman- $\alpha$  and Lyman- $\beta$  emissions from high-pressure microhollow cathode discharges in Ne H<sub>2</sub> mixtures*. *Journal of Physics B: Atomic, Molecular and Optical Physics*, 1999. **32**: p. 651-58.

3. Moselhy, M., R.H. Stark, K.H. Schoenbach, and U. Kogelschatz, *Resonant energy transfer from argon dimers to atomic oxygen in microhollow cathode discharges*. Applied Physics Letters, 2001. **78**(7): p. 880.
4. Stockhausen, G. and M. Kock, *Proof and analysis of the pendulum motion of beam electrons in a hollow cathode discharge*. Journal of Physics D: Applied Physics, 2001. **34**: p. 1683-1689.
5. Gill, P. and C.E. Webb, *Electron energy distributions in the negative glow and their relevance to hollow cathode lasers*. Journal of Physics D: Applied Physics, 1977. **10**: p. 299-311.
6. Helm, H., *Experimenteller Nachweis des Pendel-Effektes in einer zylindrischen Niederdruck-Hohlkathoden-Entladung in Argon*. Z. Naturforsch, 1972: p. 1812-1820.
7. J. W. Frame, D.J.W., T. A. DeTemple, J. G. Eden, *Microdischarge Devices Fabricated in Silicon*. Applied Physics Letters, 1997. **71**(9): p. 1165-67.
8. K. H. Schoenbach, A.E.-H., Wenhui Shi, Marco Ciocca, *High-Pressure Hollow Cathode Discharges*. Plasma Sources Science and Technology, 1997(6): p. 468-477.
9. K. H. Schoenbach, A.E.-H., Mohamed M. Moselhy, Wenhui Shi, Robert H. Stark, *Microhollow Cathode Discharge Excimer Lamps*. Physics of Plasmas, 2000. **7**(5): p. 2186-91.
10. Becker, K.H., P.F. Kurunczi, and K.H. Schoenbach, *Collisional and radiative processes in high-pressure discharge plasmas*. Physics of Plasmas, 2002. **9**(5): p. 2399.
11. Schoenbach, K.H., R. Verhappen, T. Tessnow, F.E. Peterkin, and W.W. Byszewski, *Microhollow cathode discharges*. Applied Physics Letters, 1996. **68**(1): p. 13.
12. Moselhy, M., W. Shi, R.H. Stark, and K.H. Schoenbach, *Xenon excimer emission from pulsed microhollow cathode discharges*. Applied Physics Letters, 2001. **79**(9): p. 1240.
13. Bass, A., C. Chevalier, and M.W. Blades, *A capacitively coupled microplasma (CC $\mu$ P) formed in a channel in a quartz wafer*. J. Anal. At. Spectrom., 2001. **16**(9): p. 919-921.
14. Stark, R.H. and K.H. Schoenbach, *Electron heating in atmospheric pressure glow discharges*. Journal of Applied Physics, 2001. **89**(7): p. 3568.
15. Fiala, A., L.C. Pitchford, and E.E. Kunhardt. *Two-dimensional, hybrid model of glow discharge in hollow cathode geometries in International conference on phenomena in ionized gases*. 1995. Stevens Institute of Technology; Hoboken, NJ (United States).
16. Dufour, T., R. Dussart, P. Lefaucheux, P. Ranson, L.J. Overzet, M. Mandra, J.B. Lee, and M. Goeckner, *Effect of limiting the cathode surface on direct current microhollow cathode discharge in helium*. Applied Physics Letters, 2008. **93**(7): p. 071508.
17. Kulsreshath, M.K., L. Schwaederle, L.J. Overzet, P. Lefaucheux, J. Ladroue, T. Tillocher, O. Aubry, M. Woytasik, G. Schelcher, and R. Dussart, *Study of dc micro-discharge arrays made in silicon using CMOS compatible technology*. Journal of Physics D: Applied Physics, 2012. **45**(28): p. 285202.
18. Chen, F., *Introduction to Plasma Physics and Controlled Fusion*. 2 ed. 1984, New York: Plenum Press.
19. Baalrud, S.D., J.D. Callen, and C.C. Hegna, *Instability-enhanced collisional effects and Langmuir's paradox*. Phys Rev Lett, 2009. **102**(24): p. 245005.
20. Badareu, E. and Popescu, *Researches on the Double Cathode Effect*. Journal of electronics and control, 1958. **4**(6): p. 503-514.

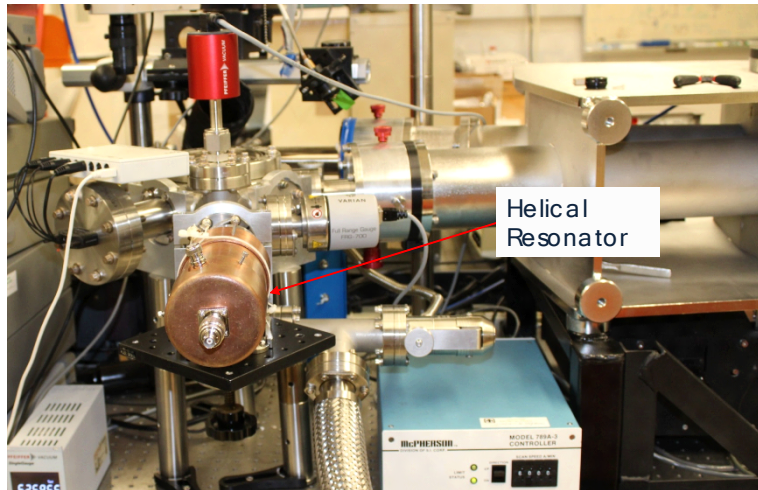
21. Gamez, G., A. Bogaerts, and G.M. Hieftje, *Temporal and spatially resolved laser-scattering plasma diagnostics for the characterization of a ms-pulsed glow discharge*. Journal of Analytical Atomic Spectrometry, 2006. **21**(3): p. 350.
22. Belenguer, P., M. Ganciu, P. Guillot, and T. Nelis, *Pulsed Glow Discharges for Analytical Applications*. Elsevier, 2009: p. 19.
23. Bolouki, N., K. Tomita, S. Hassaballa, Y. Yamagata, and K. Uchino, *Temporal evolution of electron density and electron temperature profiles in a non-thermal atmospheric-pressure plasma measured by laser Thomson scattering*. Japanese Journal of Applied Physics, 2015. **54**(1): p. 016101.
24. Kramida, A., Y. Ralchenk, J. Reader, and N.A. Team, *NIST Atomic Spectra Database* N.I.O.S.A. Technology, Editor. 2015: Gaithersburg, MD.
25. Wilkinson, P.G., *Forbidden Band Systems in Nitrogen. I. The Vegard-Kaplan System in Absorption*. The Journal of Chemical Physics, 1959. **30**(3): p. 773.
26. Flagan, R. and J. Appleton, *Excitation Mechanisms of the Nitrogen First-Positive and First-Negative Radiation at High Temperature*. The Journal of Chemical Physics, 1971. **56**(3): p. 1163-1173.
27. Itikawa, Y., M. Hayashi, A. Ichimura, K. Onda, K. Sakimoto, K. Takayanagi, M. Nakamura, H. Nishimura, and T. Takayanagi, *Cross Sections for Collisions of Electrons and Photons with Nitrogen Molecules*. Journal of Physical and Chemical Reference Data, 1986. **15**(3): p. 985.
28. Sharp, T.E., At. Data, 1971(2): p. 119.
29. Fierro, A., G. Laity, and A. Neuber, *Optical emission spectroscopy study in the VUV–VIS regimes of a developing low-temperature plasma in nitrogen gas*. Journal of Physics D: Applied Physics, 2012. **45**(49): p. 495202.





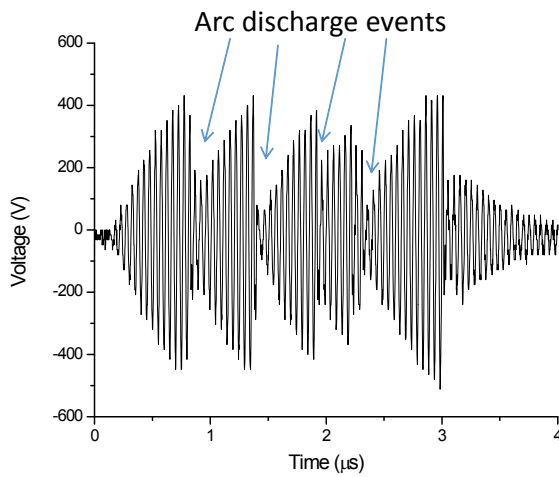
### 3. RF OPERATION

While not the original focus of this LDRD, several experiments were undertaken to understand the impact of RF operation on spectral emission and device lifetime with encouraging results on both accounts. Lifetime was increased with RF operation, while RF operation suppressed UV lines more than pulsed mode. Considering this with previous facts on pulsed operation, by proceeding from DC to short pulsed to RF operation, increasing suppression of UV lines was observed. A helical resonator was incorporated to allow RF testing as in Figure 9. The high-Q resonator converts high-power RF to high-voltage RF. An example of the voltage versus time during use of the helical resonator with the MD is shown in Figure 10.



Incorporation of a helical resonator on the test chamber bias input was used for RF driving of the MD.

**Figure 9: Test system modification for RF operation.**



3  $\mu$ s long pulses of RF at 20.3 MHz with a repetition rate of 100 Hz for a microplasma discharge in air.

**Figure 10: Example of voltage with time for RF pulsing.**

A set of experiments was conducted with 17 MHz RF applied to the MD for 4  $\mu$ s with a repetition rate of 500 Hz. As mentioned, the helical resonator converted high-power RF to high voltage RF. The voltage across and current through the MD was measured as a function of the input voltage to the RF amplifier. Note, there is no arc discharging so that the voltage and current are constant over the 4  $\mu$ s pulse. In the following set of figures, the presence of plasma does not alter the impedance of the helical resonator and MD system because the inductance of the resonator and the capacitance of the MD dominate over the much lower plasma discharge resistance. But, when the discharge resistance drops sufficiently low, the Q of the system is reduced and the applied voltage drops. Note that plasma voltages indicated are peak-to-peak. Thus to initiate plasma roughly half the voltage is required for pulsed-DC operation. Peak-to-peak voltage versus peak-to-peak current, peak-to-peak voltage versus input voltage and peak-to-peak current versus input voltage were recorded under vacuum and 655 Torr Ne conditions. Figures 11 and 12 show those results and optical images.

The spectral output of a particular MD was measured under pulsed DC and RF driving, as shown in Figure 13. RF driving was performed at an input voltage of 1.5 V (460 V<sub>pp</sub> across device) with a pulse length of 4  $\mu$ s, pulse frequency of 1 kHz and RF frequency of 17.9 MHz. The McPherson spectrometer slit width was set at 800  $\mu$ m. Further details are provided in the figure. By comparison, the pulsed spectrum was taken with 589 V across the MD at a pulse width of 300 ns, pulse frequency of 1 kHz. RF operation significantly reduces the UV line intensity.

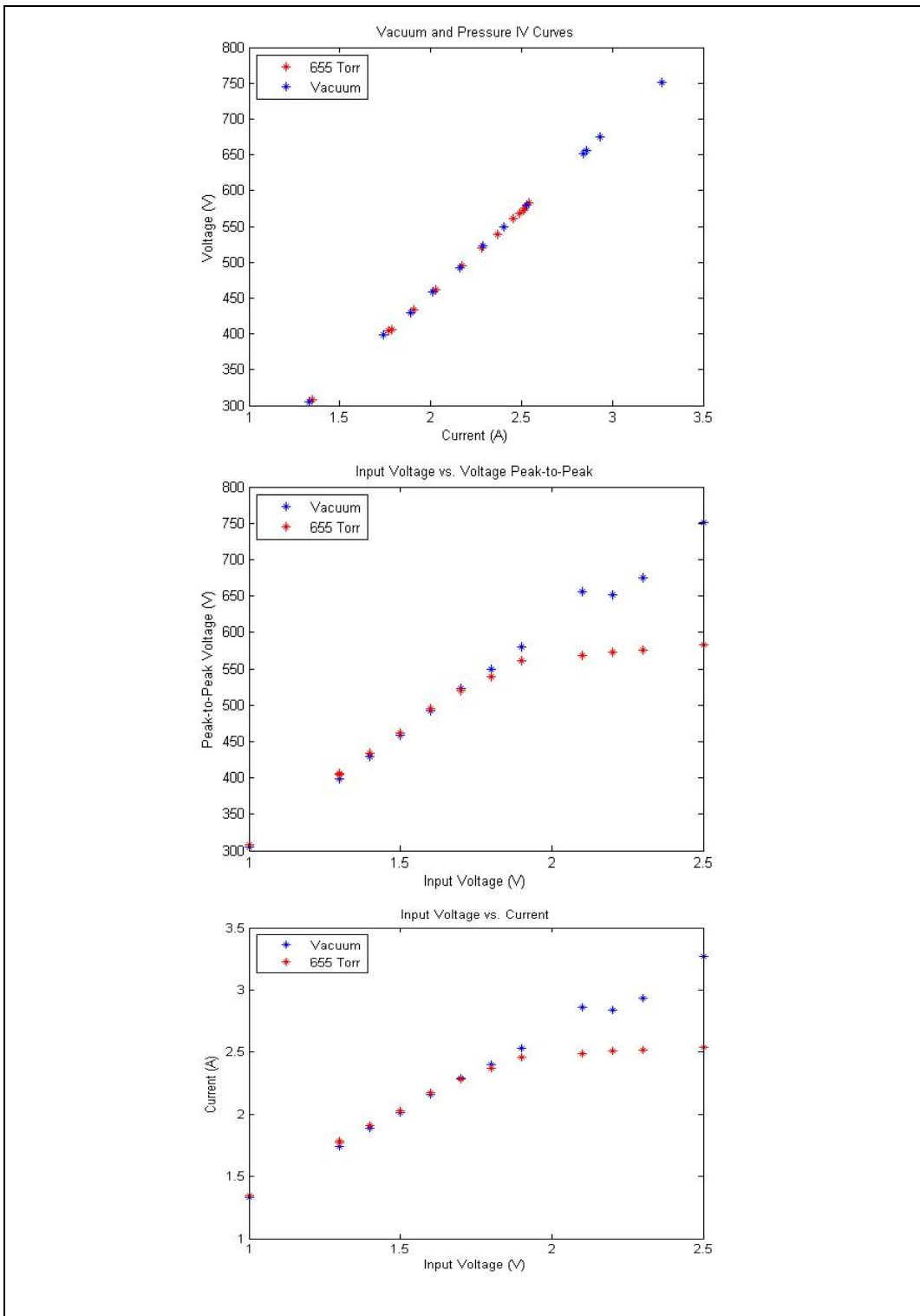
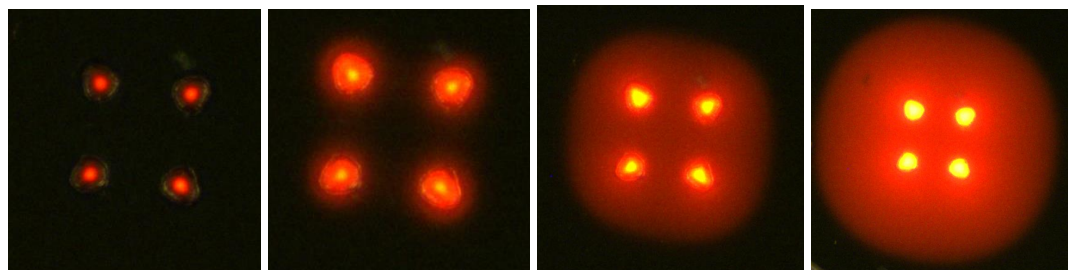
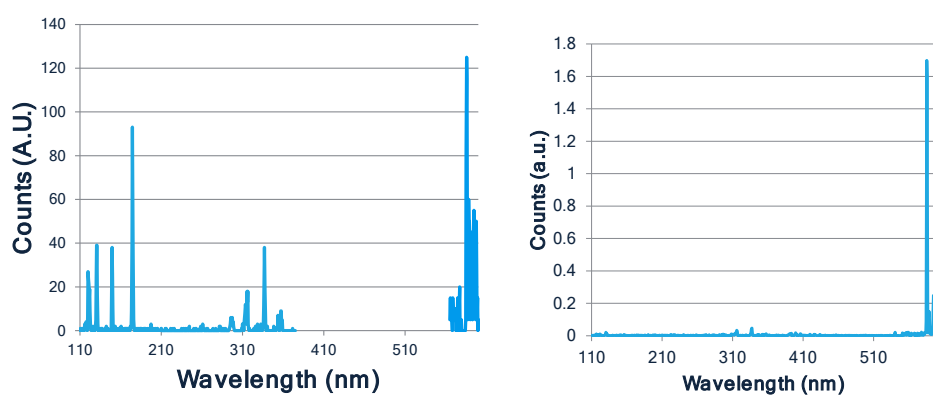


**Figure 11: RF operation.**



From left to right: Input voltage (peak-to-peak output voltage) of 1.3 V (407 V), 1.8 V (540 V), 2.2 V (575 V), 2.5 V (583 V) for the same array. (Image magnification varies from left to right.)

**Figure 12: Optical images under RF driving.**







## 4. 3D FULLY KINETIC SIMULATION OF MICROSCALE DISCHARGE

Advanced fabrication technologies can create microscale discharge devices down to size tolerances of a few microns. Such small distances allow for the generation of electric fields with modest voltages sufficient to produce glow discharges in atmospheric pressure. At atmospheric pressure collisional effects usually drive velocity distributions to continuum Maxwellian ones, but strong non-equilibrium and non-continuum effects develop here due to the high electric fields and small length scales. Understanding these non-equilibrium effects and how they are influenced by geometry and operating conditions is critical to understanding microscale discharge behavior. In this paper we describe the operation of a microdischarge device and provide a fully kinetic three-dimensional computational model of its initiation. By employing collisional Particle-in-Cell simulation techniques we capture the transient initiation and steady state behavior of the discharge, the former being a challenge or unachievable for non-kinetic methods. We provide a summary of this transient behavior and provide information that would not be available from continuum approaches.

### 4.1 Introduction

Advances in microfabrication methods have enabled the creation of micro-plasma or microdischarge (MD) devices with reliable characteristic dimensions ranging from about 10  $\mu\text{m}$  to 1 mm. Owing to their diverse applications in biomedicine, vacuum ultraviolet (VUV) light generation, pressure and chemical sensing, etc., as well as their unique physical operating principles, MDs have been intensely studied, particularly in the last quarter century [1-3]. Physical scaling laws permit microplasmas to operate around atmospheric pressure, a distinct advantage for practical use. Despite this pressure regime, local rarefaction is common and MD is characterized by rapid transient evolution, three-body collisions, extreme spatial gradients, strong convection, and non-equilibrium behavior. For these reasons and their small size, spatially- and temporally-resolved measurements are difficult to perform on MD, though recent experiments have made great strides [4-8]. Computer modeling and simulation can be a valuable means to gain insight into the physics of MD that are otherwise difficult to probe experimentally.

Initial numerical studies of MD were predominantly based on continuum fluid models [9-15]. Among other findings, these studies vividly illustrate that rapid gas convection ( $\sim 20$  m/s) is responsible for widely distributing the metastable states required for excimer creation [10], helping to explain the prevalence of VUV emission, which is one of the more promising hallmarks of MD. The primary disadvantage of such continuum studies, however, is that the electron energy distribution function (EEDF) and the trajectories of beam electrons are estimated, not explicitly calculated. Choi and Ryu performed a one-dimensional kinetic study of a direct-current (DC) plasma formed in the gap of planar electrodes separated by a 200  $\mu\text{m}$  [16]. This particle-in-cell Monte Carlo collision (PIC-MCC) simulation showed definitively that the electrons are not in thermodynamic equilibrium and the use of Maxwellian distributions in continuum models is imprecise.

Several other one dimensional PIC-MC studies have shown that the EEDF depends strongly on electrode gap and voltage, including the generation of bi-modal and tri-modal distributions [17-20]. Hong et al [20], compared PIC and fluid models of needle discharges at RF and Microwave

frequencies and found that the EEDF was trimodal at 13.56 MHz while it was more Maxwellian at 2.45 GHz. A two-dimensional axisymmetric model of direct current argon discharges in 100  $\mu\text{m}$  diameter MD at 10 and 100 Torr with a 50  $\mu\text{m}$  gap between anode and cathode was also studied by Hong et al [21]. This work nicely simulated the pendular motion of secondary electrons and studied two different secondary electron emission models, which have significant consequences for plasma density and discharge voltage.

In this paper we present the results of a 20-degree sector model on a MD 100  $\mu\text{m}$  in diameter with a 10  $\mu\text{m}$  gap between anode and cathode, similar to that which can be produced by standard microfabrication techniques. We provide a description of the computational model, specifically discussing challenges specific to 3D low temperature discharge modeling, present and discuss results from the model, and finally provide insights including those only available from kinetic models.

## 4.2 Model Description

Our modeling approach uses the Aleph simulation tool. It combines Particle-In-Cell (PIC) [1] [2], Monte Carlo Collision (MCC), and Direct Simulation Monte Carlo (DSMC) [3] methods on unstructured meshes. Aleph also includes advanced methods for dynamic particle weighting to allow us to evolve simulations with density growth over orders of magnitude. Although Aleph is typically executed in massively parallel high performance computing environments, it can also run on single cores if that is sufficient. Aleph has been extensively used for simulating a variety of low temperature plasma phenomena, and has targeted discharge processes in particular (vacuum, low pressure, atmospheric, and higher).

### 4.2.1 Physical System

Our model is motivated by experimental investigations at Sandia involving a microscale discharge device used to generate UV photons from a neon discharge. The geometry and a picture of a typically operating device are presented below in Figure 14 and the operating conditions are included in Table 1. Because the discharge experiment included a significant amount of impurities (e.g.,  $\text{O}_2$ ,  $\text{N}_2$ , and others), we do not expect quantitative comparisons with our simplified neon-only model. But by targeting the model to relevant physical parameters (geometry, length scales) we hope to provide insights valuable to model development for real systems. Note in Table 1 that “the maximum electric field” requires additional interpretation as the triple points at each dielectric edge cause locally higher fields, but only in a small region; instead, the average E field over the dielectric gap is included here.

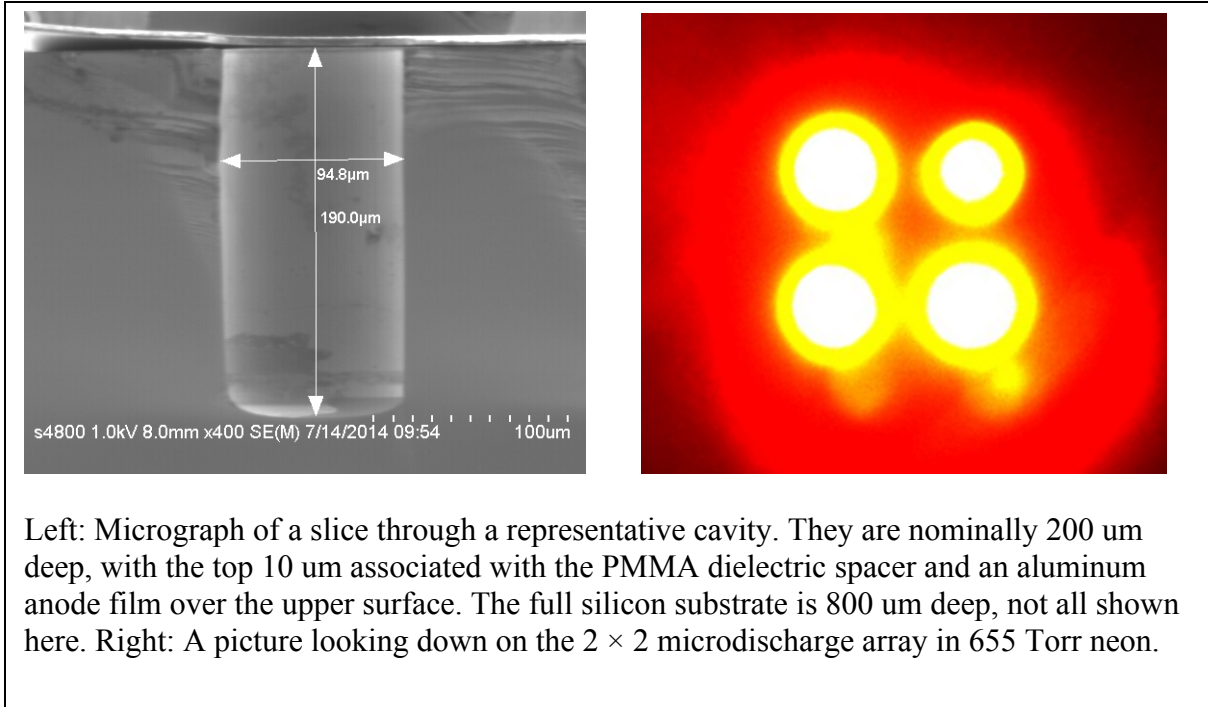


**Figure 14: SEM cross-section and Ne discharge.**

**Table 1: Physical parameters of the discharge system.**

Parameter	Value
Applied voltage	$V_{\text{PS}} = 100\text{-}1000 \text{ V}$
Gap (dielectric) length	$d_{\text{gap}} = 10 \mu\text{m}$
Maximum average applied field	$E = 10\text{-}100 \text{ MV/m}$
Gas pressure	$p_{\text{Ne}} = 655 \text{ Torr}$
Gas temperature	$T_{\text{Ne}} = 300 \text{ K}$
Gas density	$n_{\text{Ne}} = 2.1 \times 10^{25} / \text{m}^3$
Reduced field	$E/n_{\text{Ne}} = 474\text{-}4740 \text{ Td}$
Ion impact secondary emission yield at cathode	$\gamma_{\text{SE}} = 0.15$
Dielectric permittivity (polyimide)	$\epsilon_{\text{D}} = 3.0$

#### 4.2.2 Geometry and Mesh Resolution

The spatial domain is represented by a 20-degree sector (wedge) of the cylindrical geometry with artificial boundaries placed at offsets sufficiently far away from the cavity to have small effect on the simulation output. A graphical depiction of this system is shown in Figure 15. The silicon surfaces facing the gas and facing the dielectric are included in the cathode. The upper part of the device surface and the two artificial boundaries are considered the anode surface. Note that the anode film is represented as a zero thickness surface, but the dielectric is fully represented. The top and outer artificial model boundaries are 250  $\mu\text{m}$  away from the device top and centerline, respectively.

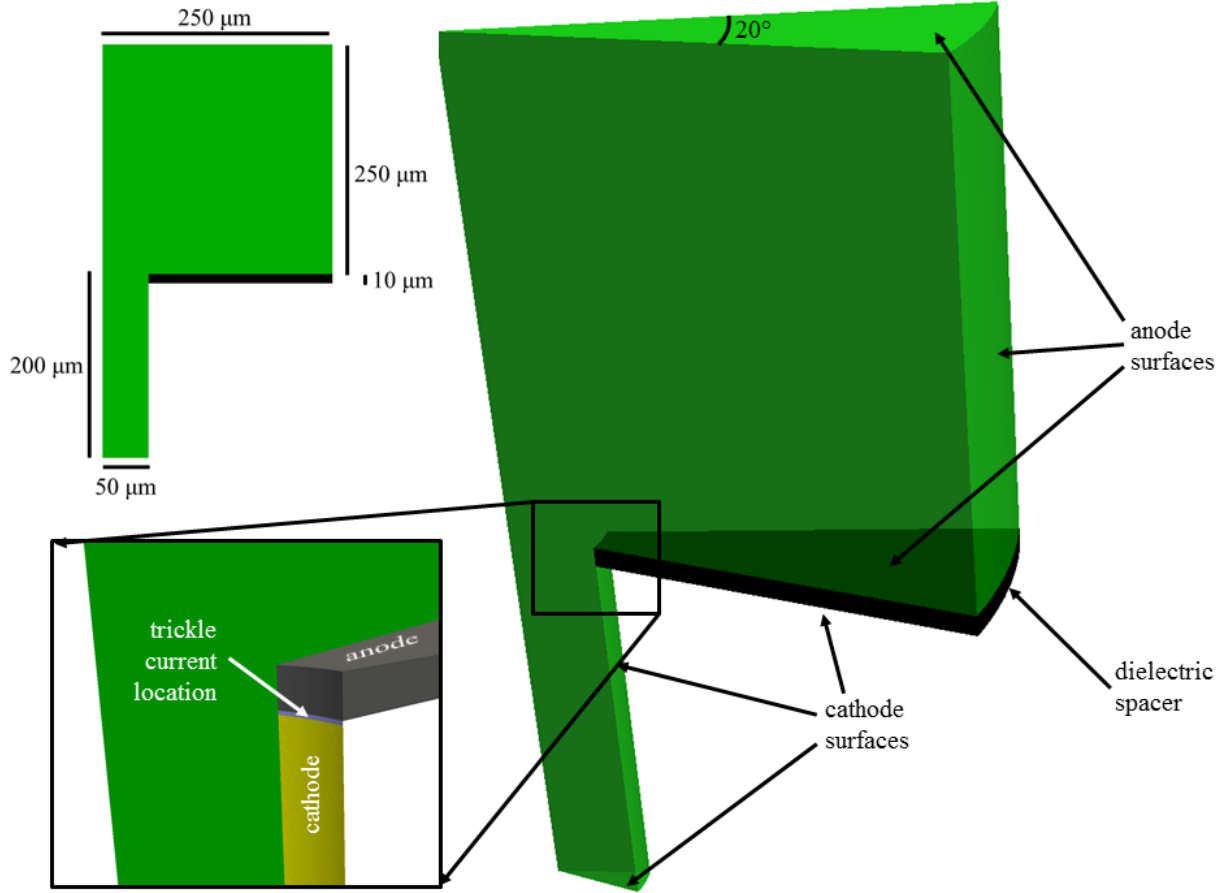


**Figure 15: 20-degree 3D sector model used for simulations.**

Aleph's use of unstructured meshes for the computational domain was developed to address the extremely broad range of spatial mesh size requirements encountered during discharge, especially vacuum discharge, due to the  $\sim 10^6$  (or higher) variation in Debye lengths and collision mean free paths encountered in these challenging systems. We take advantage of that capability for this discharge model, as can be seen in the meshes shown in Figure 16. The cavity and some distance around it is meshed with a fixed size of  $\Delta x = 1 \mu\text{m}$ . However, the cells away from the cavity, where we expect much lower plasma densities, are given increasing cell sizes, culminating in cell sizes along the outer boundary of  $\Delta x = 10 \mu\text{m}$ . The resulting savings in computational size are significant. A  $\Delta x = 1 \mu\text{m}$  mesh of fixed size everywhere contains  $\sim 27.2$  million elements, whereas our variably sized mesh contains  $\sim 3.1$  million elements, a savings of approximately a factor of 10.

Although the geometry is axisymmetric we employ a full three-dimensional model domain to demonstrate the feasibility of such a simulation, and avoid centerline ( $r = 0$ ) issues sometimes encountered in axisymmetric PIC simulations. All of the results we present are scaled to a single full cavity. For example, the electron current we collect at the anode is reported throughout this paper through a multiplicative factor of  $360/20 = 18$ . However the potential at the anode is independent of the sector angle.

Assuming a maximum  $n_e$  of  $10^{20} \text{ m}^{-3}$ , and an electron temperature of  $T_e = 2 \text{ eV}$ , we estimate the smallest Debye length to be  $\lambda_D = 1.05 \mu\text{m}$ . The mesh size of  $\Delta x = 1 \mu\text{m}$  barely resolves this. Although care is taken to understand Debye length scale resolution, estimating the Debye length actually encountered in the simulation is difficult and will be discussed below. The smallest collisional mean free path is  $1.6 \mu\text{m}$  (for electron-neutral elastic collision maximum cross section of  $\sigma_{\text{elastic,max}} = 2.9 \times 10^{-20} \text{ m}^2$ ), also resolved.

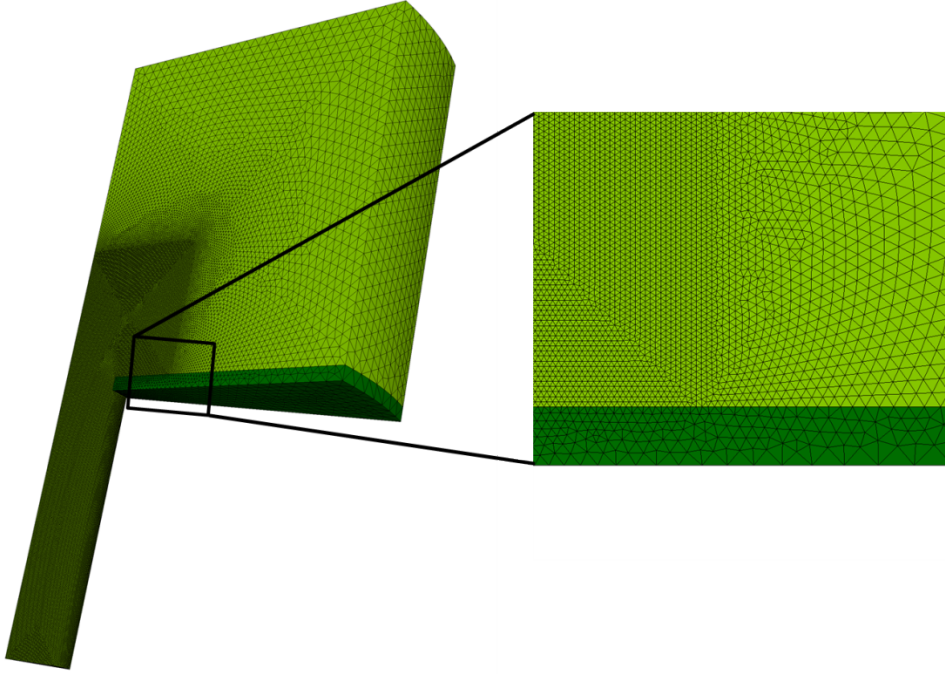


**Figure 16: Mesh used for all simulations.**

#### 4.2.3 Temporal Resolution

The constraints on the time step include resolving the plasma frequency and collision frequencies, and satisfying a particle CFL. Again assuming the maximum  $n_e$  of  $10^{20} \text{ m}^{-3}$ , resolving the plasma frequency requires a time step smaller than 3.5 ps. The other two constraints require an estimate of electron speed, which we estimate by assuming a maximum potential gain for an electron generated at the cathode reaching the anode without interactions to be 400 V (for the range of drive voltages we investigate), resulting in an electron speed of  $v_{e,\text{max}} = 12 \times 10^6 \text{ m s}^{-1}$ . Resolving the maximum collision frequency (with  $\sigma_{\text{elastic,max}}$  and  $n_{\text{Ne}}$  as above) requires a time step smaller than 140 fs. Resolving a particle CFL condition (where a particle may not move more than a characteristic cell length in a time step) with  $v_{e,\text{max}} = 12 \times 10^6 \text{ m s}^{-1}$  and  $\Delta x = 1 \mu\text{m}$  requires a time step smaller than 84 fs. Note that there are likely no electrons at the speed based on the full potential drop due to collisions, so this latter constraint is probably overly constrictive. To satisfy all of these constraints, we choose a time step of  $\Delta t = 50 \text{ fs}$ .

#### 4.2.4 Plasma Chemistry

Our model includes 8 separate atomic species:  $e^-$ , Ne,  $Ne^+$ ,  $Ne(1s_2)$ ,  $Ne(1s_4)$ ,  $Ne(1s_3)$ ,  $Ne(1s_5)$  and  $Ne(2p_1)$ . Following the model by Kushner [4], the  $Ne(1s_2)$  and  $Ne(1s_4)$  excited states (that spontaneously decay back to the ground state) are represented and tracked as one “combined” species in the simulation, which we label  $Ne(1s_{2,4})$ . Similarly, the two metastable 1s states  $Ne(1s_3)$  and  $Ne(1s_5)$  are represented as one “combined” species labelled  $Ne(1s_{3,5})$ . Although we do include radiative decay processes that generate photons, we do not include photoelectric current or present results for spectra generation. Our model includes the interactions given in Table 2 and the associated cross sections are shown in Figure 17.

**Table 2: Interactions included in the simulations.**

Interaction	Description	Source/Model
$e^- + Ne \rightarrow e^- + Ne$	elastic scattering	Biagi v8.9 database (LXcat) [5] [6]
$e^- + Ne \rightarrow e^- + Ne(1s_{2,4})$	excitation	Biagi v8.9 database (LXcat) [5] [6]
$e^- + Ne \rightarrow e^- + Ne(1s_{3,5})$	excitation	Biagi v8.9 database (LXcat) [5] [6]
$e^- + Ne \rightarrow e^- + Ne(2p_1)$	excitation	Biagi v8.9 database (LXcat) [5] [6]
$e^- + Ne \rightarrow Ne^+ + 2e^-$	ionization	Krishnakumar 1998 [7]
$e^- + Ne(1s_*) \rightarrow Ne^+ + 2e^-$	ionization	Johnson 1996 (a)
$e^- + Ne(2p_1) \rightarrow Ne^+ + 2e^-$	ionization	Johnson 1996
$Ne + Ne^+ \rightarrow Ne + Ne^+$	elastic collision	VHS [3]
$Ne(2p_1) \rightarrow Ne(1s_{2,4}) + v(585.25 \text{ nm})$	radiative emission	NIST, rate = $6.82 \times 10^7 \text{ s}^{-1}$
$Ne(2p_1) \rightarrow Ne(1s_{2,4}) + v(540.06 \text{ nm})$	radiative emission	NIST, rate = $9.00 \times 10^5 \text{ s}^{-1}$
$Ne(1s_{2,4}) \rightarrow Ne + v(73.59 \text{ nm})$	radiative emission	NIST, rate = $6.58 \times 10^8 \text{ s}^{-1}$ (b)

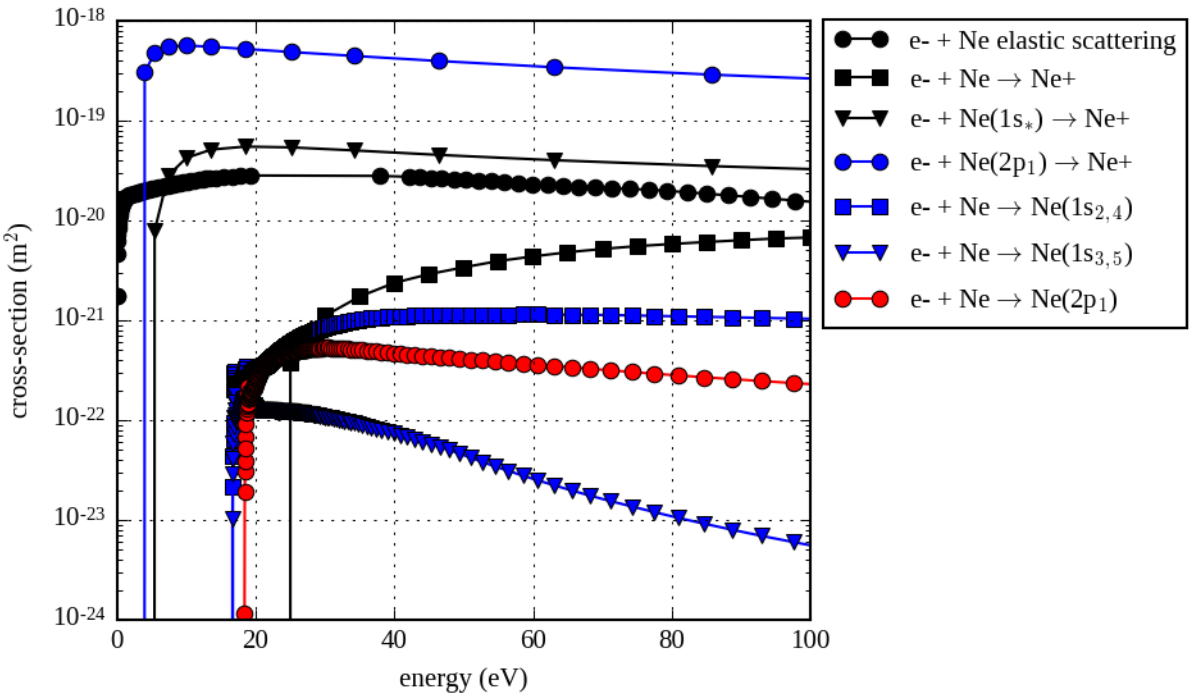


**Figure 17: Cross sections for kinetic interactions used in the model.**

#### 4.2.5 Initial Condition

The simulation is initialized with a background of Ne. Because the background density is always so much higher than the other species (by factors of at least  $10^3$ ), we model it as a constant unchanging background with fixed density  $n_{Ne} = 2.11 \times 10^{25} \text{ m}^{-3}$  and temperature  $T_{Ne} = 300 \text{ K}$  (from the physical system and incorporating  $p = 655 \text{ Torr}$ ). All other species are initially unpopulated.

#### 4.2.6 Boundary Condition

The cathode surfaces (see Figure 16) are all held grounded at  $V = 0 \text{ V}$ . Note that in the physical system there is actually a ground plane at an offset of  $675 \mu\text{m}$  at the bottom of the silicon substrate. However, the effective resistance of the silicon is negligible here ( $\sim 740 \text{ m}\Omega$ ), and the “ground plane” is instead applied at these selected model surfaces. Secondary electron emission is applied at the cathode surface, with the yield  $\gamma_{SE} = 0.15$ .

Surface charging is applied at the gas-facing dielectric surface.

A Dirichlet boundary condition model representing a simple ballast resistor circuit is applied to the anode surfaces,

$$V_A(t) = V_D - I_A(t)R_A \quad \text{\texttt{* MERGEFORMAT (1)}}$$

where  $V_D$  is the drive voltage,  $R_A$  is the ballast resistor between the power supply and anode surface,  $I_A(t)$  is the current through the anode, and  $V_A(t)$  is the resulting potential enforced at the anode surface. In all simulations,  $R_A = 332 \text{ k}\Omega$ , as was used in the experiment.  $V_D$  was varied between 150 V and 450 V. Note that  $I(t)$  must be evaluated according to incoming electron charges at the anode surface. How to do this becomes complicated in our system due to extremely small time steps and particle weights, which will be discussed below.

At  $t = 0$ , a trickle current of electrons representing 1  $\mu\text{A}$  (for a full cavity) is injected in the 1  $\mu\text{m}$  tall strip inside the cavity just below the dielectric (see Figure 16). This trickle current is maintained for 10 ns, and then shut off to allow a self-sustained discharge to form, or not. Without turning off the trickle current the anode current would be a combination of the steady discharge current and the current due to electron multiplication across the gap of the trickle current itself. Because this is a material interface (a triple point with gas, dielectric, and silicon electrode meeting at a single location), it is a likely emission location. There are multiple methods to seed electrons to initiate discharge models, including laying in initial uniform or spatially constrained neutral plasma, or an initial population of only electrons. We chose the trickle current instead of one of these other methods because it has a physical basis (emission from a triple point), and its magnitude (current) can be compared directly to steady behavior. Typical final currents are  $\sim 300 \mu\text{A}$  (for a full cavity).

#### 4.2.7 Particle Weights

Determining particle weights is one of the most challenging steps for this class of three-dimensional low temperature plasma models. The extra challenge due to simulating in three dimensions is significant, is not encountered in lower dimensional systems, and has not been well explored.

First, we note that our plasma parameter (number of electrons within a Debye sphere),

$$\Lambda = n_e \frac{4}{3} \pi \lambda_D^3 \quad \text{\texttt{* MERGEFORMAT (2)}}$$

is  $\sim 490$ , giving us confidence that we are still in the regular plasma regime, as opposed to a strongly coupled plasma.

The small cell sizes encountered in the three-dimensional system are the root cause of many of the computational challenges. The volume of a tetrahedron with edge length  $\Delta x = 1 \mu\text{m}$  is  $\sim 1.2 \times 10^{-19} \text{ m}^3$ , and actual cell sizes are often somewhat smaller (a hexahedron, as encountered in a regular Cartesian mesh with the same  $\Delta x$ , would have a volume of  $10^{-18} \text{ m}^3$ , of course). For purposes of discussion, we assume a typical tetrahedral element volume of  $10^{-19} \text{ m}^3$ . In contrast, for a two-dimensional system using SI units where the “in plane” dimension is taken to be 1 m deep, the volume of a cell based on a triangular element is  $\sim 4.3 \times 10^{-13} \text{ m}^3$ . This is significant because it puts a bound on the minimally resolvable number and charge density represented by a single computational particle. Given a computational particle weight of 1 (a reasonable smallest particle weight), computed  $n_e$  and  $\rho$  will always be of magnitude 1/volume, or  $\sim 10^{19} \text{ m}^{-3}$  or

larger. In contrast, particle weights of 1000 result in minimally resolvable densities of  $\sim 4.3 \times 10^{16} \text{ m}^{-3}$  in the two-dimensional system. This difference has significant impact: the latter (two-dimensional) minimal charge density resolution may represent negligible space charge, while the former (three-dimensional) minimum charge density resolution may represent very significant space charge.

A potential mitigation to this “quantized” charge effect is to apply spatial and/or temporal smoothing methods. The consequences of employing these methods is very problem dependent, and in the end one would like to apply as little smoothing as possible and not trade off accuracy for artificial stabilization. Employing computed intensive (volume-dependent) quantities such as  $n_e$ ,  $\rho$ , etc., suffering from this quantization effect must be carefully assessed. They can easily result in unexpected algorithmic departures. We note that Aleph’s electrostatic solution method is finite element based, and the computed  $\rho$  is multiplied by the volume of the cell in the solution process, returning to a value of charge independent of cell volume. We have learned, however, to avoid using a spatially smoothed  $\rho$  via cell-to-node-to-cell averaging as this resulted in overly noisy effective charge densities due to adjacent cells having different volumes. This problem would apply to spatially smoothing any intensive quantity (e.g., density). Again, the three-dimensional aspect of the simulation worsened the problem; the same  $\Delta x$  change in adjacent cells results in a larger volume change in three dimensions than two. Note that smoothing for output purposes has no algorithmic impact.

Given the above considerations, we chose to employ electron particle weights of 1 (one computational particle represents one real particle). The ground state Ne background is represented as a uniform background density, and the electron-neutral interactions create products of weight equal to the electron, and no mass is removed from, nor energy correction applied to, the Ne. Product densities do not exceed 0.1% of the background neutral density so the loss of background Ne is negligible. Aleph uses a dynamic particle weighting capability (based on merging pairs of particles close to each other in velocity space), which increases particle weights to maintain particle count limits, which we set to be 72 per cell for electrons, and 36 per cell for all other species (it is effectively inactive until densities build up in the simulation).

Finally, returning to the calculation of  $I(t)$  for use in the resistor-in-series circuit model, we note that a single electron charge  $q_e$  hitting the anode in one 50 fs time step represents a current of 3.2  $\mu\text{A}$ . Given that the steady currents are only 100 times larger, we desired a smaller representable current and choose to average the anode current over 160 ps so that each impacting electron contributes 1 nA per time step while it is included in the running average. A better, more physical model, would appear to require significant development to properly represent the circuit response, and beyond a simple RLC implementation using a smoothed  $I(t)$ , which we did not explore here.

### 4.3 Results and Discussion

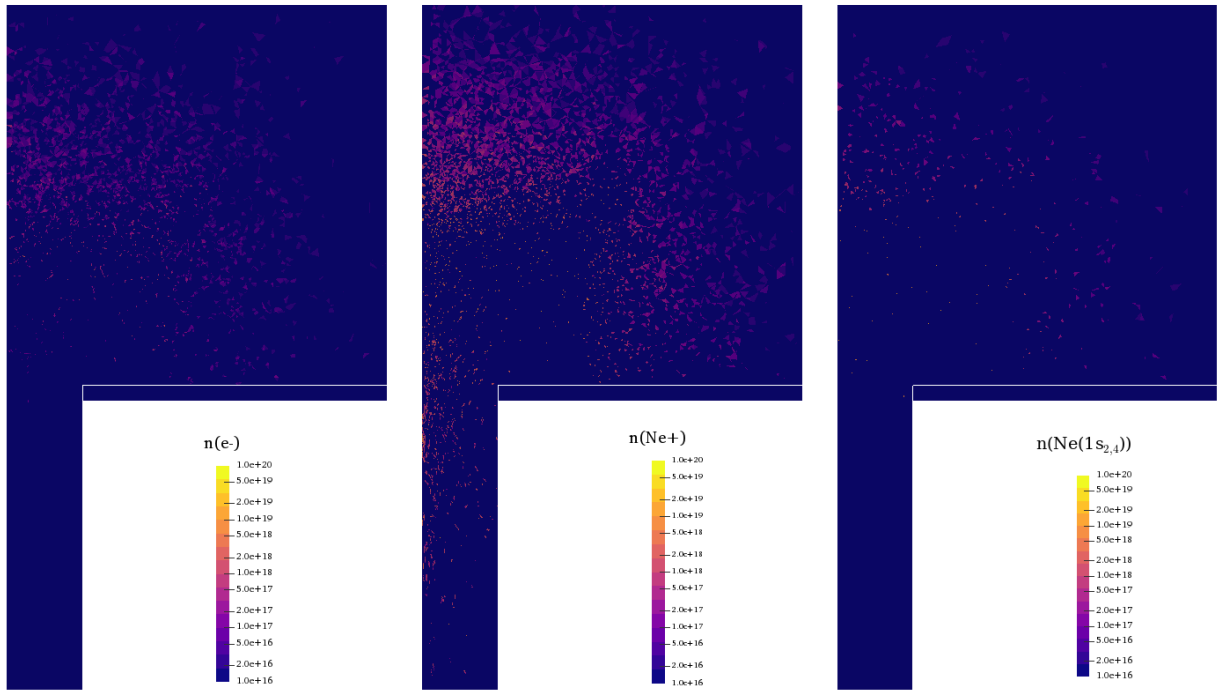
We simulate the temporal evolution of the 20-degree wedge system at voltages ranging from 150-400 V in 50 V increments. The simulations consumed 512 cores of CPU time for 96-144 hours (two or three 48 hour sequences, using a full particle restart capability). A typical progression of species densities are shown in Figure 18, and potentials and fields in Figure 20, all

for the  $V = 250$  V drive voltage case. Other voltages share the same qualitative behavior, but result in increasing maximum plasma densities. In Figure 18 slices were taken through the midplane of the domain. All density scales are logarithmic from  $1016$  to  $1020$   $\text{m}^{-3}$ . The times correspond to (top)  $t = 10$  ns (when the trickle current is turned off), (middle)  $t = 55$  ns (in the middle of the breakdown), (bottom)  $t = 100$  ns, and (d)  $t = 200$  ns (evidence that steady state has been achieved). Visual artifacts due to the mesh size variation can be seen (e.g., compare (d)  $\text{Ne}^+$  map to the mesh in Figure 16), but do not impact the computation.

From Figure 18 we can see the electron density is quite concentrated in a small region along the  $r = 0$  (or  $x = 0$ ) axis, at a height approximately equal to the dielectric. This is consistent with the location of the maximum fields near the dielectric separator. The ions are more spread out than the electrons -- this is attributed to the increased mobility of the electrons constraining them closer to the peak potential and the more strongly driven  $\text{Ne}^+$  flow (discussed below).

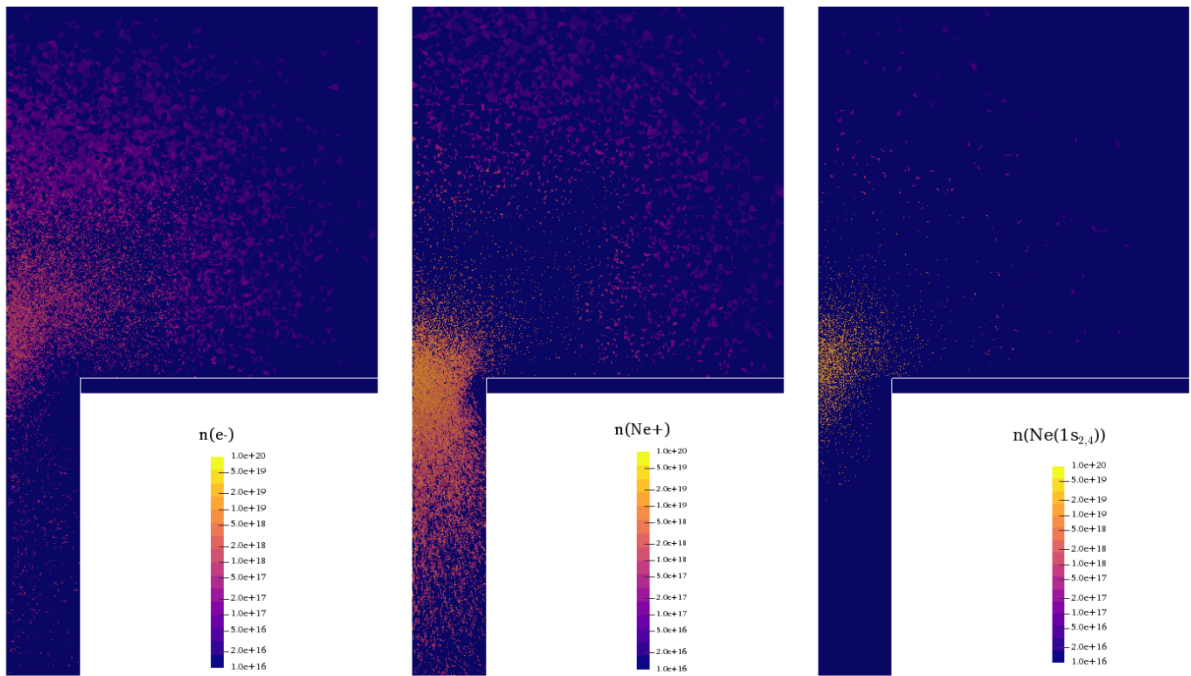
The excited state distribution is a function of competing processes: generation through electron impact (should approximately correlate to electron density), diffusion of the species, and radiative decay of the species. A 300 K neutral neon has a RMS speed of  $0.525$   $\mu\text{m/ns}$ . A length scale of  $10$   $\mu\text{m}$  (the dielectric separation distance) can thus be traversed through diffusion alone in  $20$  ns. The radiative decay rate of  $6.58 \times 10^8$   $\text{s}^{-1}$  for the  $\text{Ne}(1s_{2,4})$  excited state gives a mean lifetime of  $1.52$  ns, or mean distance travelled of  $0.800$   $\mu\text{m}$ . The mean lifetime and distance travelled before decaying for  $\text{Ne}(2p_1)$  are  $14.7$  ns and  $7.68$   $\mu\text{m}$ , respectively. The longer lifetime of  $\text{Ne}(2p_1)$  results in a larger spread in the density, as shown in Figure 19. Note also that decay from  $\text{Ne}(2p_1)$  to  $\text{Ne}(1s_{2,4})$  also occurs, but is less dominant than  $\text{Ne}(1s_{2,4})$  generation through electron impact excitation. In Figure 19 the left, middle, right species are  $\text{Ne}(1s_{2,4})$ ,  $\text{Ne}(1s_{3,5})$  and  $\text{Ne}(2p_1)$ , respectively. All ranges are logarithmic from  $10^{16}$ - $10^{20}$   $\text{m}^{-3}$ . Note the  $\text{Ne}(1s_{3,5})$  is a metastable species whereas the others radiatively decay.

The initial  $t = 0$  and final  $t = 200$  ns potentials and fields are shown in Figure 20. Note the range for potential has been shortened to highlight the region in the vicinity of the denser plasma. As shown in Figure 20 (left pane of (middle)) there is a region at the top of the denser plasma where ions will flow up, away from the cathode. The range for potentials (left panes) is  $100$ - $150$  V, to highlight the potential fields near the denser plasma region after breakdown. The range for the fields are  $-10^7$ - $10^7$   $\text{V/m}$ . The field across the dielectric is equal to  $2.5 \times 10^7$   $\text{V/m}$  at  $t = 0$ .



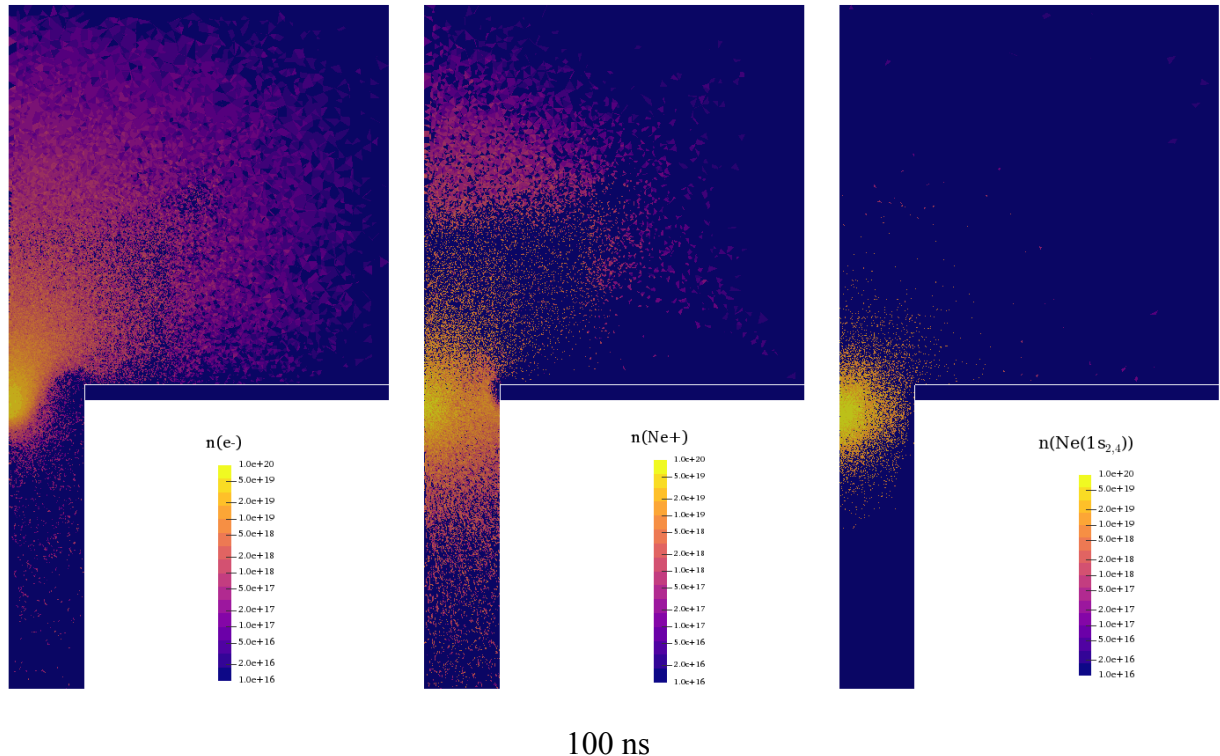
10 ns

---

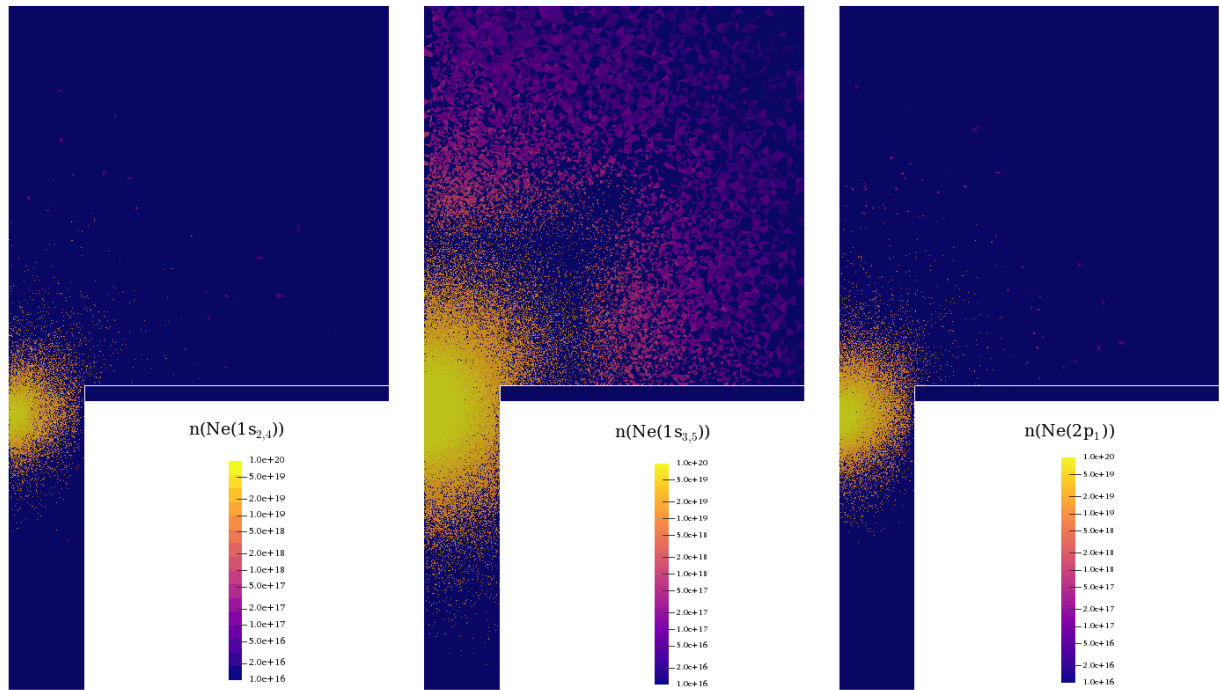


55ns

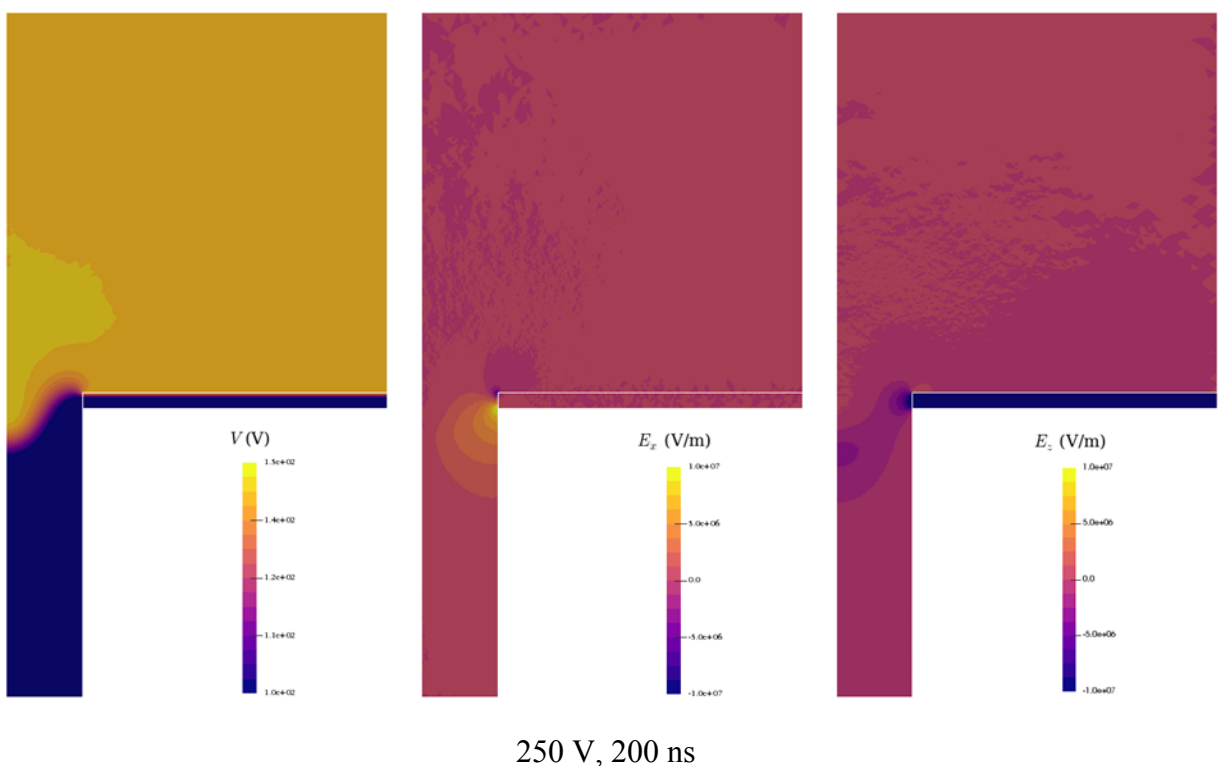
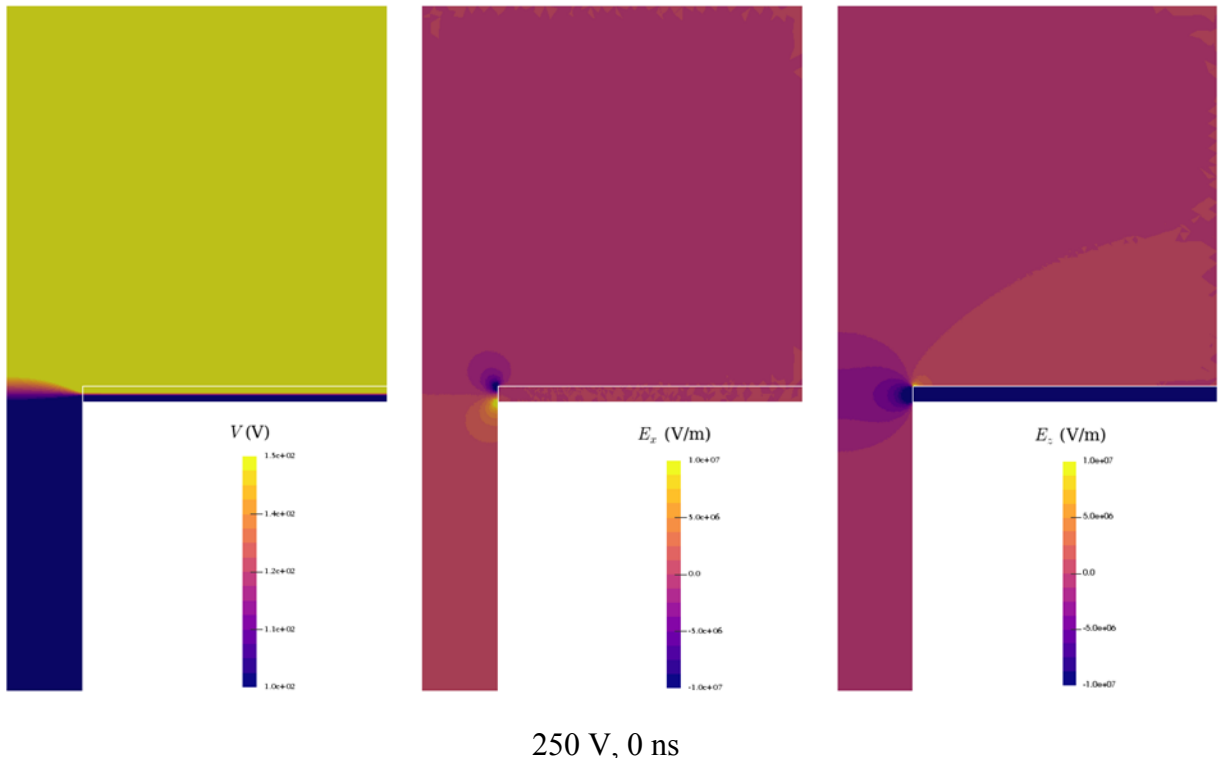
---



**Figure 18: Progression of number densities for  $e^-$ ,  $Ne^+$ , and  $Ne(1s_{2,4})$  for  $V = 250$  V drive voltage.**



**Figure 19: Comparison of excited state densities at  $t = 200$  ns for  $V = 250$  V drive voltage.**



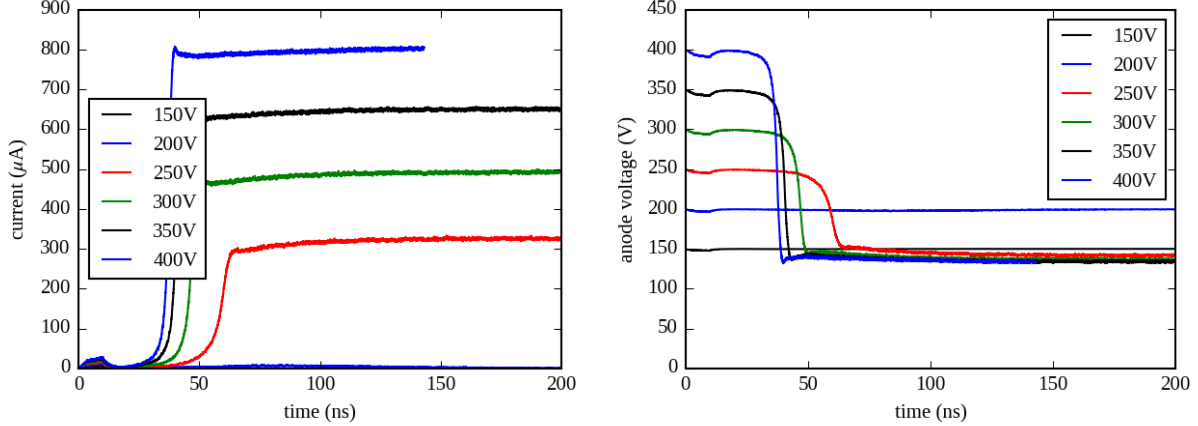
**Figure 20: Initial  $t = 0$  ns and final  $t = 200$  ns potentials and fields for  $V = 250$  V drive voltage.**

Figure 21 shows the transient behavior for the anode current and anode potential for each simulated drive voltage. All drive voltage cases show initial growth in anode current while the 1  $\mu$ A trickle current is active (the first 10 ns). When the trickle current is extinguished the system either breaks down (grows rapidly in current) or extinguishes and the temporarily supported charged species dissipate. The exact voltage where this occurs, the breakdown voltage, is not computed precisely through simulation. However, the currents in Figure 21 indicate a breakdown voltage between 200 V and 250 V; the current for the 200 V drive voltage case returns to 0 indicating it has failed to become self-sustaining, whereas the 250 V drive voltage case does break and the operating voltage converges to a fixed value. We estimate a theoretical breakdown voltage from Paschen's model,

$$V_b = \frac{Bpd}{\ln(Apd) - \ln[\ln(1 + \gamma_{SE}^{-1})]}$$

with  $A = 4.4 \text{ Torr}^{-1} \text{ cm}^{-1}$ ,  $B = 111 \text{ V Torr}^{-1} \text{ cm}^{-1}$  for neon (from [8] based on data from [8]), and the parameters Table 1, finding  $V_b = 210 \text{ V}$ . To within the +/- 50 V variation in applied voltages in the simulation we find somewhat surprising agreement considering the simulation violates many assumptions of the Paschen model: the discharge is not occurring between two parallel electrodes, the discharge is not one-dimensional, not every electron produced in the discharge necessarily reaches the anode, and not every ion produced in the discharge necessarily reaches the cathode. Note that the reduced field at the lowest drive voltage of 150 V is 711 Td, normally a field that would cause considerable electron chemistry (excitation, ionization) normally associated with breakdown, but is not sufficient here to cause breakdown. There may be more nuanced issues with the origination of the electrons. However, unless there was a continued source of electrons, or a much larger initial population of electrons, we don't believe breakdown will occur at those low voltages.

When the system breaks down, there is a period following the trickle current, but before the rapid increase in anode current, that shows nearly zero anode current (e.g., between 10 ns and 50 ns for the 250 V drive voltage case in Figure 21). This represents the time required for the initial wave of ions to transit to the cathode and generate secondary electrons at the surface. In simpler discharge geometries, this period can exhibit current oscillations as the initial processes of avalanche ionization followed by ion transit followed by another wave of avalanche ionization are separable; here the geometry and fields are sufficiently complex that it appears smooth throughout, even though the same basic mechanisms are active. The bumps at 10 ns in Figure 21 correspond to terminating the 1  $\mu$ A trickle current.



**Figure 21: Time histories of currents and anode potentials for each of the simulated voltages.**

Figure 21 shows a characteristic overshoot for the three highest voltages. We believe this is also seen experimentally but did not pursue the feature in depth. Figure 21 clearly shows a plateau effect as the applied voltage exceeds the simulation breakdown voltage. This is consistent with the behavior of a normal glow discharge: once discharge has occurred at the simulation breakdown voltage, increasing the applied voltage causes an increase in the anode current, but the plasma potential remains essentially fixed. We expect this behavior to continue until the system enters the abnormal glow discharge regime, when the steady state potential must increase to extract more current. This latter behavior is also associated with increasing plasma density.

The velocity distribution functions (VDFs) for e- and Ne+ at steady state for the  $V = 250$  V drive voltage case are shown for three different regions in Figure 22. The highest region is  $[50 \mu\text{m} < z < 100 \mu\text{m}, r < 50 \mu\text{m}]$ , the middle region is  $[-30 \mu\text{m} < z < 10 \mu\text{m}, r < 25 \mu\text{m}]$ , and the lowest region is  $[-200 \mu\text{m} < z < -100 \mu\text{m}, r < 50 \mu\text{m}]$ . These plots are not normalized for the number of samples, allowing us to see the relatively high and low particle densities in the separate regions. Note, the slice was taken from the  $V = 250$  V drive voltage case at  $t = 300$  ns. The e- VDFs are all on the same scale. The Ne+ VDFs all have different ranges due to the relatively large ranges in the simulation data. In particular, the lower region has 492, or 1.13% the number of electrons that the middle region has (43,538), even though it encompasses 10 times the volume. We see that the electrons are essentially Maxwellian, due to scattering with the background atmospheric pressure Ne. The ions, however, exhibit very interesting kinetic anisotropy. Note that the ranges on each of the three ion VDF plots are different, due to the large differences in the  $v_r$  and  $v_z$  components in the three different regions. From the mid and low region VDFs we see that the ion energy is strongly directed down and “outwards” towards larger radii. This likely would contribute to the distribution of damage after repeated use of such devices.

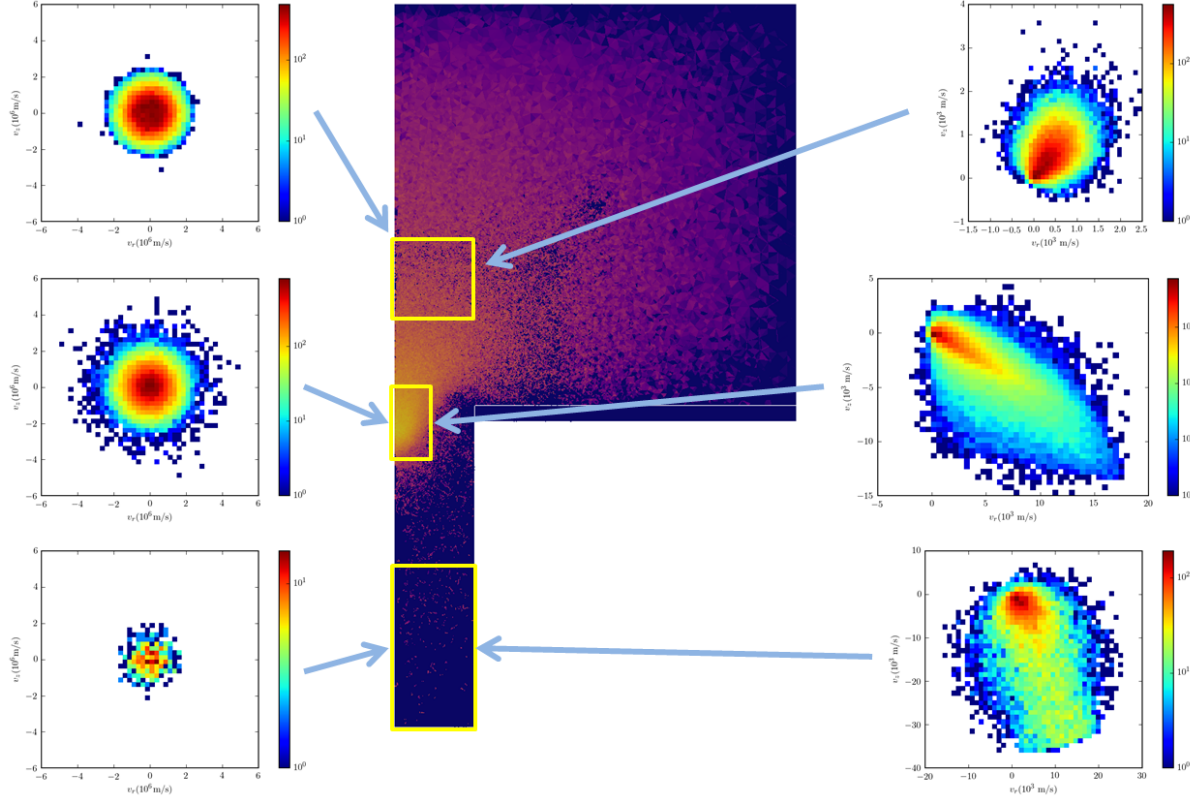


**Figure 22: Velocity distribution functions for e- (left) and Ne+ (right) for three regions, as marked on the e- density plot.**

#### 4.4 Conclusions of the 3D Model and Simulation

We have demonstrated a truly 3D kinetic model for the simulation of a physically appropriate atmospheric microscale discharge. Returning to the challenge of 3D low temperature plasma simulation and contrasting the computational vs. physical numbers of particles prompts a philosophical question. The bottom 100  $\mu\text{m}$  of the cavity in this 20-degree model only has  $\sim 500$  *physical* electrons (the particle weight remains very nearly exactly 1 even though dynamic particle weighting was active). Can this system really be properly described with a continuum model where number density is employed as the primitive variable of the solution? If the number density is claimed to be, say,  $n_e = 10^{17} \text{ m}^{-3}$ , then a 20  $\mu\text{m}$  radius circular cavity of height 20  $\mu\text{m}$  (reasonable scales for such devices) contains  $\sim 2,500$  physical electrons. Perhaps continuum models still produce some useful information, but this “model applicability” question should be raised for any nuanced information extraction from such models. For example, if a Cartesian grid with grid size of 1  $\mu\text{m}$  is employed for “high accuracy”, an actual 3D grid volume will contain, on average, 0.1 physical electrons. Any complicated models that use  $n_e = 10^{17} \text{ m}^{-3}$  from that calculation may be making inappropriate assumptions.

Even in kinetic models such as this one using a computational particle weight, sometimes called a “macroparticle weight”, of unity is outside of usual PIC-DSMC modeling experience and

prompts new concerns, such as using intensively computed quantities in an algorithmic way. Usage of integrated quantities, such as current to a surface, may be less sensitive to this “extreme” discretization (although the very small timesteps used to simulate these systems prompts other questions). Even interpreting output can be challenging -- to temporally accumulate (or smooth) data for viewing purposes may require so much data aggregation to achieve enough samples that important information is lost.

## 4.5 References for Section 4

1. K. H. Schoenbach et al, IEEE J. Quantum Electronics, 48 (2012).
2. K. H. Becker et al, J. Phys. D Appl. Phys., 39 (2006).
3. F. Iza et al, Plasma Process. Polym., 5 (2008).
4. J. C. Stephens et al, IEEE Trans. Plasma Science, 42 (2014).
5. D. Rydberg et al, Review of Scientific Instruments, 85 (2014).
6. J. C. Stephens et al, Plasma Sources Sci. Technol., 24 (2015).
7. J. C. Stephens et al, J. Phys. D Appl. Phys., 47 (2014).
8. M. K. Kulsreshath et al, J. Phys. D Appl. Phys., 45 (2012).
9. M. J. Kushner, JAP, 95 (2004).
10. M. J. Kushner, J. Phys. D: Appl. Phys, 38 (2005).
11. J. P. Boeuf et al, APL, 86 (2005).
12. J. J. Shi and M. G. Kong, “Cathod fall characteristics in a dc atmospheric pressure glow discharge,” J. Appl. Phys., 94 (9) pp 5504-5513, Aug. 2003.
13. P. S. Kothnur, X. Yuan, L. L. Raja, “Structure of direct-current microdischarge plasmas in helium,” Appl. Phys. Lett., 82 (4), pp 529-531, Jan. 2003.
14. Q. Wang, D. J. Economou and V. M. Donnelly, “Simulation of a direct current microplasma discharge in helium at atmospheric pressure,” J. Appl. Phys., 100 (2) p. 023 301, July 2006.
15. J. H. Seo and J. G. Eden, “Two-dimensional simulation of ac-driven microplasmas confined to 100-300 micron diameter cylindrical microcavities in dielectric barrier devices,” J. Appl. Phys., 100 (12) p. 123 302, Dec. 2006.
16. J. Choi, F. Iza, J. K. Lee, C-M Ryu, IEEE Trans. Plasma Sci., 35 (2007).
17. Zhang, Bogaerts jAP 2014 PIC MC 1D argon rf glow discharge limit – calculate EEDF and e temperature with gap and pressure- three different EEDF depending on gap and voltage – important role of secondary electrons
18. Zhang, Bogaerts J Phys D 2014; 1D pic mc;  $10^{18}$ - $10^{23}$  densities and bimodal at 10 um gap, rf and DC trimodal at 200 um gap
19. Moore, 2012, explicit electrostatic PIC with DSMC 1d dc air at STP. Various gap sizes compared with data and paschen curve. Cold field electron emission can explain brekdon voltage deviation from PAasch in small gaps.
20. Y. J. Hong et al, J. Phys. D Appl. Phys., 41 (2008).
21. Y. J. Hong et al, J. Korean Physical Society., 53 (2008).

## 5. CONCLUSIONS

We studied for the first time the temporal evolution of spectral lines from microplasma devices (MD), including transitions to impurity states. Impurities are expected in applications of MD so this study is important for the practical use of MD and for fundamental understanding of MD dynamics. We demonstrated that long wavelength plasma emission lines diminish more rapidly than deep UV lines with decreasing pulse width. RF operation suppresses UV emissions even further relative to pulsed operation. This means that by switching from DC to pulsed mode, or better yet for device lifetime, pulsed to RF operation, we can restrict deep UV emissions from MD. This then allows for real-time tuning of the ionization energy of a microplasma photo-ionization source. This is useful in chemical detection for selecting which chemicals are ionized. In atomic physics, this can be used to probe deep UV transitions with selectivity, such as the 27-Al atomic clock transition.

Scaling physics allows MD to operate near atmospheric pressure. Enhanced collisions in this regime, relative to low-pressure operation, allows for efficient creation of excimer states that emit down to 65 nm. Lasers fall off strongly below 200 nm due to materials limitations. New atom clocks and chemical sensing applications need wavelengths  $< 160$  nm. This LDRD and prior work by other groups show that MD can produce significant light output in this regime.

In order to understand the physics of MD, we developed the first fully kinetic 3D model with trends matching experiment. Continuum models, previously developed by other groups, estimate the electron energy distribution function. Using kinetic methods, we explicitly calculated the EEDF, which is very significant because it is non-Maxwellian with high energy components reaching 20 eV. This effect, and non-continuum effects were studied with the model/simulation and how they are impacted by geometry & driving in transient (which is not possible non-kinetically) and steady-state operation. Finally, we developed a global model to comprehend broad effects in electric field and emission from microplasmas.





## APPENDIX1: GLOBAL MODEL

A global model is a zero-dimensional model of a plasma which assumes spatial homogeneity. While it cannot capture the full complexity of a real plasma, it is suitable for basic characterization of the plasma chemistry dynamics. The simplicity of a global model provides for fast solutions and fast iteration on the plasma chemistry model which makes it particularly advantageous for situations such as this where the gas composition is fairly complex. This made the development of a global model a natural first step toward understanding the behavior of the microdischarge.

### A1.1 Model Equations

Most global models involve two governing equations, one for the number densities of the atomic and molecular species, and another to follow the evolution of the electron energy in the system. The former can be generally expressed as:

$$\frac{dn}{dt} = G - L$$

where  $n$  represents the density for some species of interest,  $G$  is the rate at which the species is produced, and  $L$  is the rate at which the species is lost. Gain and loss mechanisms vary greatly depending on the system in question and may represent excitation, ionization, detachment, or spontaneous emission among many other processes. The reactions included in the present model are described in more detail below. The gain and loss mechanisms are typically expressed as some rate constant,  $k$ , multiplied by the densities of the reactants. The units of  $k$  may vary depending on the number of bodies participating in the reaction.

The gain or loss terms may also represent physical processes that are not related to particle-particle interactions. One such example is the outflux of particles from the system. Despite the assumption of a zero-dimensional system, the microdischarge has boundaries which result in the outflux of particles from the region of concern. We describe this with a simple model based on the Bohm flux [Chen1984] at a surface, taking the positive ion flux to be equal to  $0.61n_iAc_s$ , where  $n_i$  is the ion density,  $A$  is the characteristic collection area, and  $c_s$  is the Bohm velocity for the ion in question. The collection area is assumed to be the internal area of the microdischarge geometry. Additionally, we ignore complications in the Bohm criterion related to the presence of multiple ion species [Baalrud2009]. Finally, we assume that the outflux of electrons is equal to the total outflux of ions.

The dynamics of the electron energy are considered using the equation,

$$\frac{dT_e}{dt} = \frac{2}{3k_B n_e} \left[ \frac{e^2 n_e E(t)}{m_e K_m n_g} - 3n_e K_m n_g \frac{m_e}{m_g} \frac{3}{2} k_B (T_e - T_g) - \sum \Delta \epsilon \right]$$

Here,  $T_e$  is the electron temperature,  $k_B$  is Boltzmann's constant,  $n_e$  is the electron density,  $E$  is the (time-dependent) applied electric field,  $K_m$  is the (temperature-dependent) momentum

transfer rate,  $n_g$  is the neutral gas density,  $T_g$  is the gas temperature, and  $\Delta\varepsilon$  is the energy change as the result of some reaction. The three terms in this equation represent the electron energy gained by the field, the energy loss due to neutral collisions, and the energy gained (or lost) due to reactions involving electrons.

The above equations provide the foundation for the global model. Provided initial conditions, a set of reactions with associated rate or cross section data, and an electric field, we may solve for the evolution of the excited states in the system.

## A1.1 Reactions

The reactions implemented in the global model along with their rates or cross section references are provided in Table 3. Several commendable compilations and models were used in the assembly of the reaction data [1]–[6]. A total of 27 species are considered with 47 potential reactions. Rate constants are given in units of  $\text{m}^3\text{s}^{-1}$  unless otherwise noted. When a rate constant is omitted, rates were calculated from cross section data. Neon states are given using Paschen notation. Excited states of molecular nitrogen are in the triplet manifold. Excited atomic hydrogen, oxygen, and nitrogen are those states contributing to observed VUV emissions.

The number of reactions considered is small relative to a “complete” set, however the small quantities of the molecular species, the short timescale, and the desire to simply establish a qualitative understanding led to the omission of many reactions considered to be of secondary importance. The presented reactions emphasize direct excitation of emitting states and other processes that are believed to be important to the observed behavior (resonant energy transfer [25], dissociative excitation, and excimer formation).

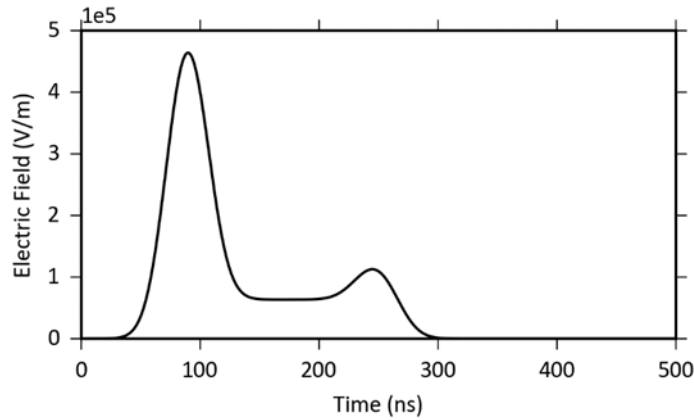
## A1.2 Solutions

The equations for particle densities and electron energy were solved using the SciPy [27] implementation of the Dormand and Prince Runge-Kutta method of order 8(5, 3) [28]. The applied electric field shape was chosen to be consistent with the observed emission dynamics. Briefly, the emissions are observed to peak soon after the pulse is applied. This is followed by a decline to relatively constant emission, ending with a peak after the applied voltage has gone to zero. The initial peak is believed to be caused by high fields in the bulk of the device prior to the formation of significant space charge. As the plasma density increases to the point where it can shield out the applied field, much of the potential drop is removed to the boundary of the plasma, thus reducing the field experienced by the bulk of the plasma.

**Table 3: Reaction rates used in the Global Model**

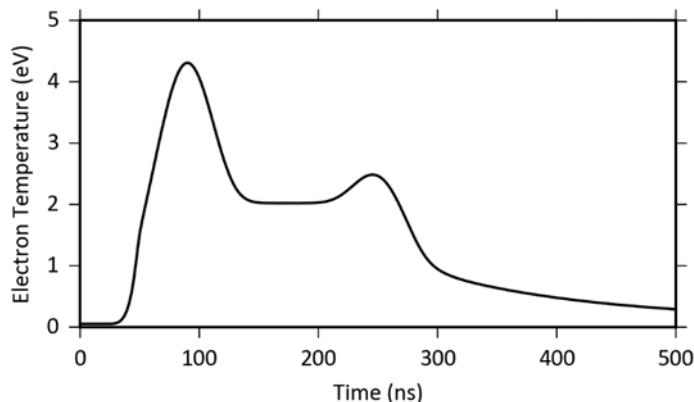
	Reaction	Rate	Ref.	Comments
Atomic Neon				
1	$e^- + Ne \rightarrow Ne + e^-$	-	[7]	
2	$e^- + Ne \rightarrow Ne(1s_5) + e^-$	-	[7]	
3	$e^- + Ne \rightarrow Ne(1s_3) + e^-$	-	[7]	
4	$e^- + Ne \rightarrow Ne(2p_1) + e^-$	-	[7]	
5	$e^- + Ne \rightarrow Ne(1s_2) + e^-$	-	[7]	
6	$Ne(1s_2) \rightarrow Ne$	$6.11 \times 10^8 \text{ s}^{-1}$	[2]	
7	$Ne(2p_1) \rightarrow Ne(1s_2)$	$6.82 \times 10^7 \text{ s}^{-1}$	[2]	
8	$e^- + Ne \rightarrow Ne^+ + e^- + e^-$	-	[7]	
9	$e^- + e^- + Ne^- \rightarrow Ne(2p_1) + e^-$	$5.0 \times 10^{-39} T_e^{-4.5}$	[1]	All recombination assumed to go to $Ne(2p_1)$
10	$Ne(1s_2) + Ne(1s_2) \rightarrow Ne^+ + Ne + e^-$	$3.2 \times 10^{-16}$	[8]	
11	$Ne(1s_2) + Ne(1s_3) \rightarrow Ne^+ + Ne + e^-$	$3.2 \times 10^{-16}$	[8]	
12	$Ne(1s_2) + Ne(1s_5) \rightarrow Ne^+ + Ne + e^-$	$3.2 \times 10^{-16}$	[8]	
13	$Ne(1s_3) + Ne(1s_3) \rightarrow Ne^+ + Ne + e^-$	$3.2 \times 10^{-16}$	[8]	
14	$Ne(1s_3) + Ne(1s_5) \rightarrow Ne^+ + Ne + e^-$	$3.2 \times 10^{-16}$	[8]	
15	$Ne(1s_3) + Ne(1s_5) \rightarrow Ne^+ + Ne + e^-$	$3.2 \times 10^{-16}$	[8]	
16	$Ne(1s_5) + Ne + Ne \rightarrow Ne_2^* + Ne$	$3.05 \times 10^{-45} \text{ m}^6 \text{s}^{-1}$	[9]	
17	$Ne(1s_5) + Ne + Ne \rightarrow Ne_2^* + Ne$	$4.98 \times 10^{-45} \text{ m}^6 \text{s}^{-1}$	[9]	
Molecular Neon				
18	$e^- + Ne_2^* \rightarrow Ne + Ne + e^-$	$1.0 \times 10^{-13}$	[1]	
19	$e^- + Ne_2^* \rightarrow Ne_2^+ + e^- + e^-$	$9.75 \times 10^{-15} T_e^{0.71} \exp(-3.4/T_e)$	[10]	
20	$e^- + Ne_2^+ \rightarrow Ne(2p_1) + Ne$	$1.7 \times 10^{-13} T_e^{-0.43}$	[11]	All recombination assumed to go to $Ne(2p_1)$
21	$Ne_2^* \rightarrow Ne + Ne$	$3.6 \times 10^8 \text{ s}^{-1}$	[12]	
22	$Ne_2^* + Ne_2^* \rightarrow Ne_2^+ + Ne + Ne + e^-$	$1.0 \times 10^{-17}$	[1]	
Atomic Hydrogen				
23	$e^- + H \rightarrow H + H^*$	-	[13]	
24	$H^* \rightarrow H$	$4.70 \times 10^8 \text{ s}^{-1}$	[14]	
Molecular Hydrogen				
25	$e^- + H_2 \rightarrow e^- + H + H$	-	[6]	Dissociation cross section minus (27)
26	$e^- + H_2 \rightarrow e^- + H^* + H$	-	[15]	Emission cross section for Lyman- $\alpha$
27	$e^- + H_2 \rightarrow e^- + H_2^+ + e^-$	-	[6]	Total ionization cross section
Atomic Oxygen				
28	$e^- + O \rightarrow e^- + O^*$	-	[5]	
29	$O^* \rightarrow O$	$3.41 \times 10^8 \text{ s}^{-1}$	[16]	
Molecular Oxygen				
30	$e^- + O_2 \rightarrow e^- + O + O$	-	[17]	Dissociation minus (32)
31	$e^- + O_2 \rightarrow e^- + O^* + O$	-	[18]	Emission cross section
32	$e^- + O_2 \rightarrow e^- + O^+ + e^-$	-	[4]	Total ionization cross section
Atomic Nitrogen				
33	$e^- + N \rightarrow N^* + e^-$	-	[19]	
34	$N^* \rightarrow N$	$4.07 \times 10^8 \text{ s}^{-1}$	[20]	
Molecular Nitrogen				
35	$e^- + N_2 \rightarrow e^- + N + N$	-	[3]	Total dissociation cross section for neutral products minus (37)
36	$e^- + N_2 \rightarrow e^- + N^* + N$	-	[21]	
37	$e^- + N_2 \rightarrow e^- + N_2(A)$	-	[3]	
38	$e^- + N_2 \rightarrow e^- + N_2(B)$	-	[3]	
39	$e^- + N_2 \rightarrow e^- + N_2(C)$	-	[3]	
40	$e^- + N_2 \rightarrow e^- + N_2^+ + e^-$	-	[3]	Total ionization cross section
41	$N_2(C) \rightarrow N_2(B)$	$2.39 \times 10^7 \text{ s}^{-1}$	[22]	$v=0$
42	$N_2(B) \rightarrow N_2(A)$	$8.85 \times 10^4 \text{ s}^{-1}$	[23]	$v=0$
Mixed				
43	$Ne^+ + N_2 \rightarrow N_2^+ + Ne$	$2.9 \times 10^{-18}$	[24]	
44	$Ne_2^* + H_2 \rightarrow Ne + Ne + H + H^*$	$3.0 \times 10^{-17}$	[25]	
45	$Ne_2^* + O_2 \rightarrow Ne + Ne + O + O^*$	$3.0 \times 10^{-17}$	[25]	Assumed the same as hydrogen
46	$Ne(1s_3) + N_2 \rightarrow N_2^+ + e^- + Ne$	$8.4 \times 10^{-17}$	[26]	Assumed same as $1s_5$
47	$Ne(1s_5) + N_2 \rightarrow N_2^+ + e^- + Ne$	$8.4 \times 10^{-17}$	[26]	

Figure 23 depicts the applied field for one of the simulations. The width of the depicted pulse is 160 ns, however all simulations featured the same field for the first peak, the intermediate period, and the final peak: 22 Td, 3 Td, and 5 Td respectively. The width of the pulses at the beginning and end of the discharge period are set to be 30 ns based on the observed emission behavior. In the case of the first peak, this is believed to represent the period of time necessary for space charge to become significant and the intermediate steady state to establish. The amplitude of the fields were selected on the basis that they produced similar temperatures and densities to Thomson scattering measurements of a similar discharge [29].



**Figure 23: Electric field applied for the simulations of 160 ns pulselength.**

The electron energy distribution was assumed to be Maxwellian and can be seen in Figure 24 for the 160 ns case. It is probable that this assumption is not accurate during the initiation of the microdischarge given the large reduced electric fields. This will most likely result in an underestimate of the excitation rates for higher levels. Future simulations could be improved by the use of approximate solutions to the Boltzmann equation or Monte-Carlo methods to establish more accurate electron energy distribution functions for use in the rate calculations. Ultimately, kinetic simulations of the actual geometry will be required to understand the potential impact of non-local electron kinetics.



**Figure 24: Electron temperature for a 160 ns pulselength simulation.**

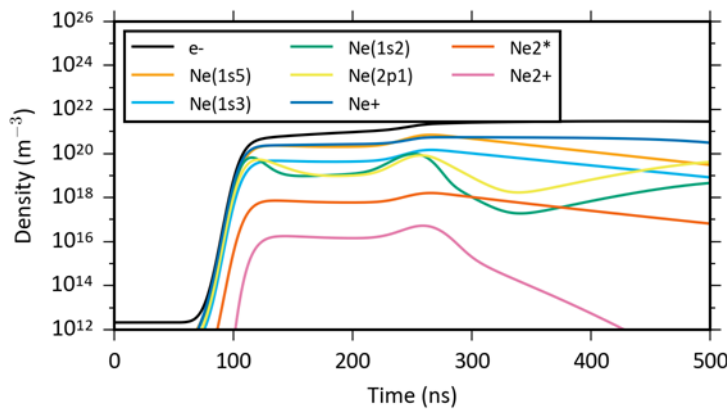


**Figure 25: The evolution of the electron and neon species densities of the 160 ns pulse.**

Figure 25 depicts the dynamics of the excited neon states. For reference, a density of  $10^{12}$  is approximately equal to a single particle in the volume of the microdischarge device. The model is initialized with an ionization fraction of  $10^{-13}$  representing a negligible amount of preionization. The electron density grows rapidly accompanied by the atomic states of neon. The neon excimer and molecular ion states take longer to populate owing to the prerequisite excited states of atomic neon. The post-pulse rise in  $\text{Ne}(1s_2)$  and  $\text{Ne}(2p_1)$  states can be attributed to the recombination of neon ions into excited neon states.

Lastly, the global model is able to provide the time evolution of emissions from the discharge. These are shown in Figure 26. Several additional radiative transitions are tracked by the model as detailed in the reactions table, here the transitions plotted are those for which experimental data were available. For each transition, the values have been normalized to the amplitude of the first peak. It should be noted that the radiative transition rates used were those for *untrapped* emissions. In reality, the VUV emissions are all resonance radiation which should be treated appropriately. However, given the complex geometry and unknown densities of atomic oxygen, hydrogen, and nitrogen in the volume between the discharge and the spectrometer window no accounting was made for this effect. In reality, trapping would be expected to increase the effective lifetime of the trapped states shifting the peaks of these emissions relative to untrapped transitions such as  $\text{Ne}(2p_1) \rightarrow \text{Ne}(1s_2)$ .

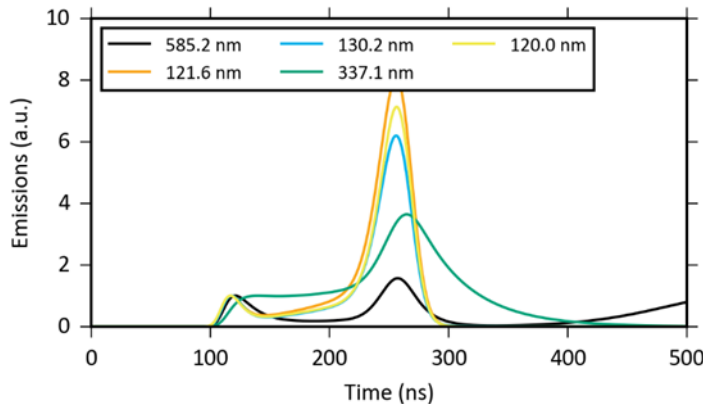


**Figure 26: Emission dynamics determined by the global model for the 160 ns pulse width.**

### A1.3 References for Appendix I

- [1] M. J. Kushner, “Modeling of microdischarge devices: Pyramidal structures,” *J. Appl. Phys.*, vol. 95, no. 3, pp. 846–859, 2004.
- [2] A. Kramida, Y. Ralchenko, and J. Reader, “NIST Atomic Spectra Database (version 5.3),” 2016. [Online]. Available: <http://www.nist.gov/pml/data/asd.cfm>. [Accessed: 20-Aug-2016].
- [3] Y. Itikawa, “Cross sections for electron collisions with nitrogen molecules,” *J. Phys. Chem. Ref. Data*, vol. 35, no. 1, pp. 31–53, 2006.
- [4] Y. Itikawa, “Cross sections for electron collisions with oxygen molecules,” *J. Phys. Chem. Ref. Data*, vol. 38, no. 1, pp. 1–20, 2009.
- [5] Y. Itikawa and A. Ichimura, “Cross Sections for Collisions of Electrons and Photons with Atomic Oxygen,” *J. Phys. Chem. Ref. Data*, vol. 19, no. 3, pp. 637–651, 1990.
- [6] J.-S. Yoon, M.-Y. Song, J.-M. Han, S. H. Hwang, W.-S. Chang, B. Lee, and Y. Itikawa, “Cross Sections for Electron Collisions with Hydrogen Molecules,” *J. Phys. Chem. Ref. Data*, vol. 37, no. 2, pp. 913–931, 2008.
- [7] O. Zatsarinny and K. Bartschat, “Large-scale pseudostate calculations for electron scattering from neon atoms,” *Phys. Rev. A - At. Mol. Opt. Phys.*, vol. 85, no. 6, pp. 1–8, 2012.
- [8] V. A. Sheverev, V. P. Stepaniuk, and G. G. Lister, “Chemi-ionization in neon plasma,” *J. Appl. Phys.*, vol. 92, no. 7, pp. 3454–3457, 2002.
- [9] C. O. Akoshile, J. D. Clark, and J. Cunningham, “Reactions of excited neon atoms in neon-helium afterglows. I. Rate data,” *J. Phys. B At. Mol. Phys.*, vol. 18, no. 13, pp. 2793–2803, Jul. 1985.
- [10] S. Rauf and M. J. Kushner, “Dynamics of a coplanar-electrode plasma display panel. II. Cell optimization,” *J. Appl. Phys.*, vol. 85, no. 7, p. 3470, 1999.
- [11] L. Frommhold, M. A. Biondi, and F. J. Mehr, “Electron-Temperature Dependence of Electron-Ion Recombination in Neon,” *Phys. Rev.*, vol. 165, no. 1, pp. 44–52, Jan. 1968.
- [12] J. S. Cohen and B. Schneider, “Ground and excited states of Ne2 and Ne2+.II. Spectroscopic properties and radiative lifetimes,” *J. Chem. Phys.*, vol. 61, no. 8,

p. 3230, 1974.

[13] R. K. Janev and J. J. Smith, “Cross Sections for Collisions Processes of Hydrogen Atoms with Electrons, Protons and Multiply Charged Ions,” *APID (Volume 4)*, 1993.

[14] J. Baker, “Transition Probabilities for One Electron Atoms,” Washington, D.C., 2008.

[15] H. Tawara, Y. Itikawa, Y. Itoh, T. Kato, H. Nishimura, S. Ohtani, H. Takagi, K. Takayanagi, and M. Yoshino, “Atomic Data Involving Hydrogens Relevant to Edge Plasmas,” Nagoya, JP, 1986.

[16] A. Hibbert, M. Godefroidp, and N. Vaeckjj, “El transitions of astrophysical interest in neutral oxygen,” *Glass*, vol. 24, pp. 3943–3958, 1991.

[17] P. C. Cosby, “Election-impact dissociation of oxygen,” *J. Chem. Phys.*, vol. 98, no. 12, pp. 9560–9569, 1993.

[18] I. Kanik, C. Noren, O. P. Makarov, P. Vattipalle, J. M. Ajello, D. E. Shemansky, T. Oi, and H. S. Telescope, “Electron impact dissociative excitation of O 2 : 2. Absolute emission cross sections of the OI(130.4 nm) and OI(135.6 nm) lines,” *J. Geophys. Res.*, vol. 108, no. E11, pp. 1–10, 2003.

[19] Y. Wang, O. Zatsarinny, and K. Bartschat, “B -spline R -matrix-with-pseudostates calculations for electron-impact excitation and ionization of nitrogen,” *Phys. Rev. A - At. Mol. Opt. Phys.*, vol. 89, no. 6, pp. 1–12, 2014.

[20] G. I. Tachiev and C. Froese Fischer, “Breit-Pauli energy levels and transition rates for nitrogen-like and oxygen-like sequences,” *Astron. Astrophys.*, vol. 385, no. 2, pp. 716–723, Apr. 2002.

[21] J. F. M. Aarts and F. J. De Heer, “Emission cross sections for NI and NII multiplets and some molecular bands for electron impact on N2,” *Physica*, vol. 52, no. 1, pp. 45–73, Mar. 1971.

[22] F. Valk, M. Aints, P. Paris, T. Plank, J. Maksimov, and A. Tamm, “Measurement of collisional quenching rate of nitrogen states N2(C3Πu,v=0) and N+2(B2Σ+g,v=0),” *J. Phys. D. Appl. Phys.*, vol. 43, no. 38, p. 385202, 2010.

[23] F. R. Gilmore, R. R. Laher, and P. J. Espy, “Franck–Condon Factors, r-Centroids, Electronic Transition Moments, and Einstein Coefficients for Many Nitrogen and Oxygen Band Systems,” *J. Phys. Chem. Ref. Data*, vol. 21, no. 5, p. 1005, 1992.

[24] T. D. Märk and H. J. Oskam, “Production and loss of N 2 + , Ne+ and Ne 2 + during the decay period of plasmas produced in neon-nitrogen mixtures,” *Zeitschrift für Phys.*, vol. 247, no. 1, pp. 84–94, Feb. 1971.

[25] J. Wieser, M. Salvermoser, L. H. Shaw, A. Ulrich, D. E. Murnick, and H. Dahi, “Lyman-alpha emission via resonant energy transfer,” *J. Phys. B At. Mol. Opt. Phys.*, vol. 31, no. 20, pp. 4589–4597, 1998.

[26] J. M. Brom, J. H. Kolts, and D. W. Setser, “Quenching rate constants for Ne3P2) metastable atoms at room temperature,” *Chem. Phys. Lett.*, vol. 55, no. 1, pp. 44–48, 1978.

[27] E. Jones, T. Oliphant, and P. Peterson, “SciPy: Open Source Scientific Tools for Python,” 2001. [Online]. Available: <http://www.scipy.org>. [Accessed: 20-Aug-2016].

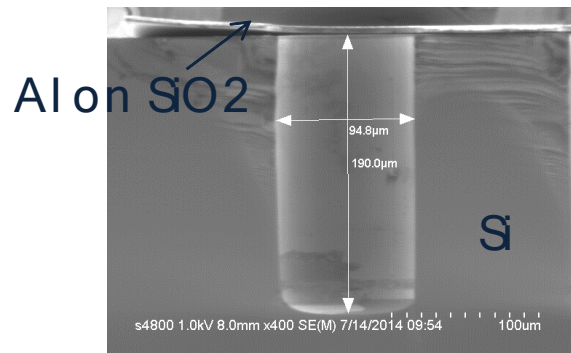
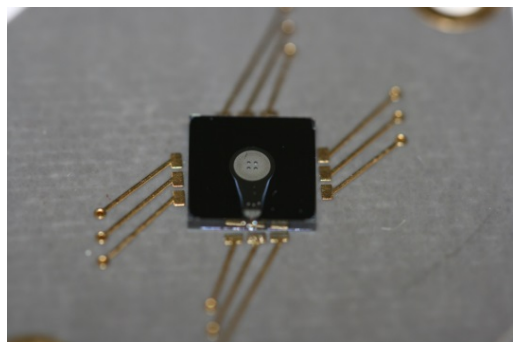
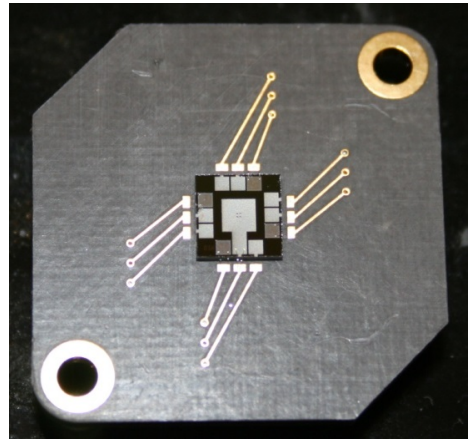
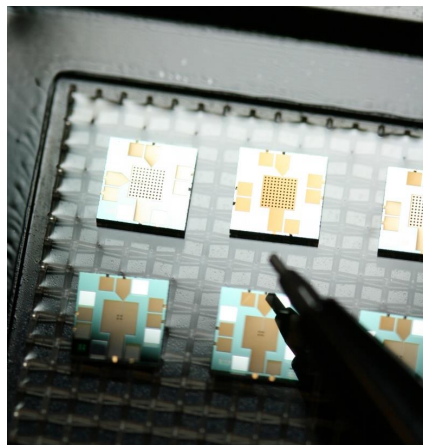
[28] E. Hairer, S. P. Norsett, and G. Wanner, *Solving Ordinary Differential Equations I. Nonstiff Problems*, 2nd ed. Springer-Verlag, 1993.

[29] N. Bolouki, K. Tomita, S. Hassaballa, Y. Yamagata, and K. Uchino, “Temporal evolution of electron density and electron temperature profiles in a non-thermal atmospheric-pressure plasma measured by laser Thomson scattering,” *Jpn. J. Appl. Phys.*, vol. 54, no. 1, p. 16101, Jan. 2015.



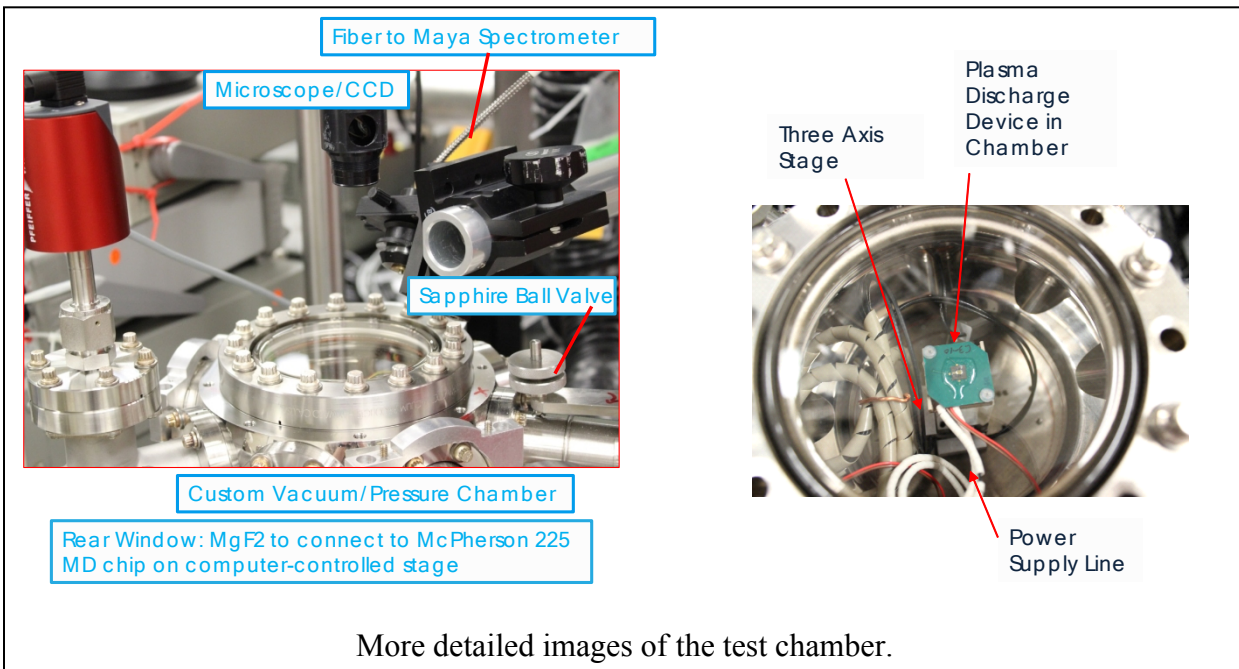
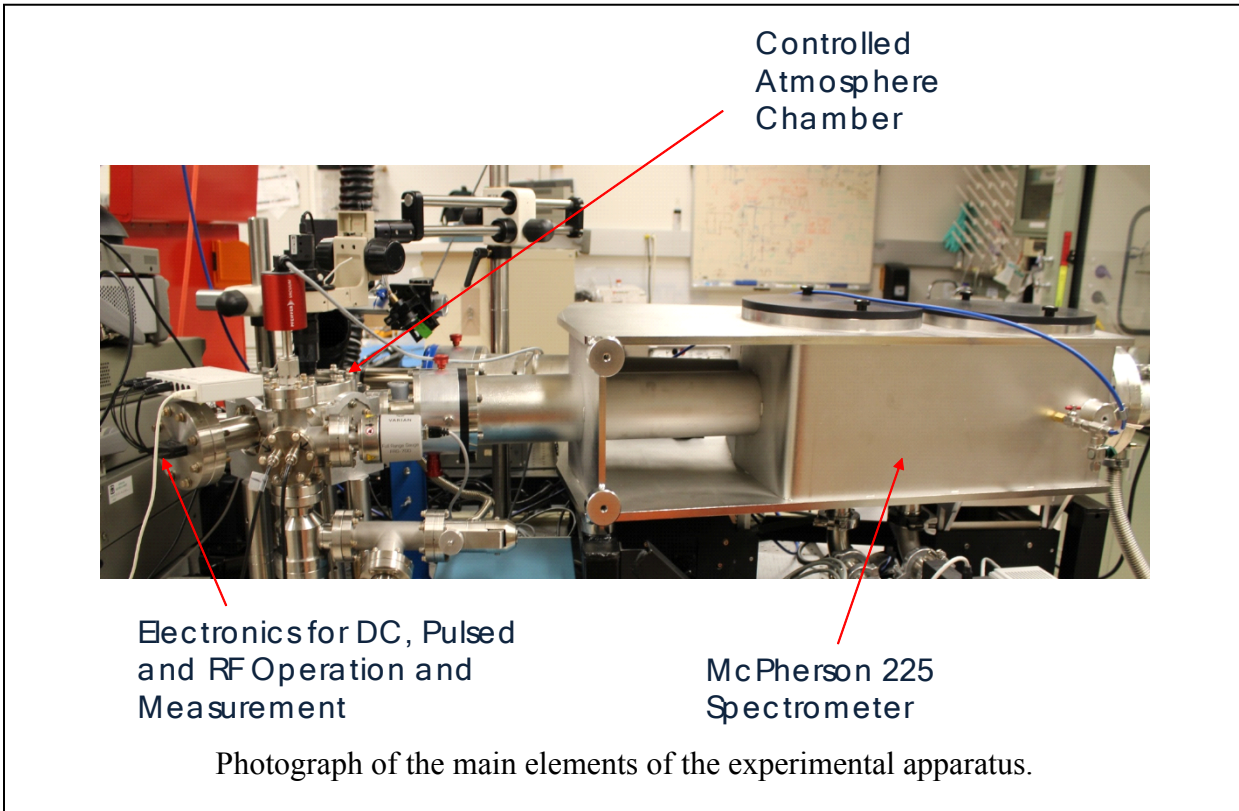
## APPENDIX 2: ADDITIONAL IMAGES

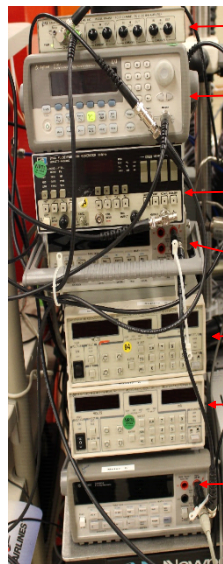
### A2.1 Device images



The top row shows originally designed devices with arrays from 4 to 100 devices. The lower left is a revised design with a circular top anode and 4 MD. The lower right is a cross section SEM view of a MD.

## A2.2 System images





Stanford SR445A DC Amplifier

Agilent 33210A

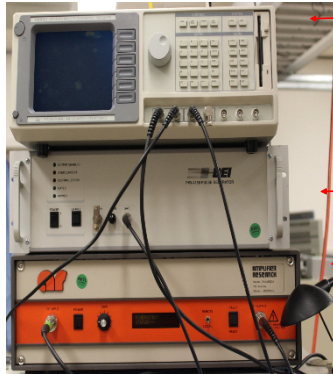
HP 8116A Pulse/Function Generator

HP 34401A Multi-Meter

Stanford PS350 Power Supply

Stanford PS350 Power Supply

Agilent 34401A Multi-Meter



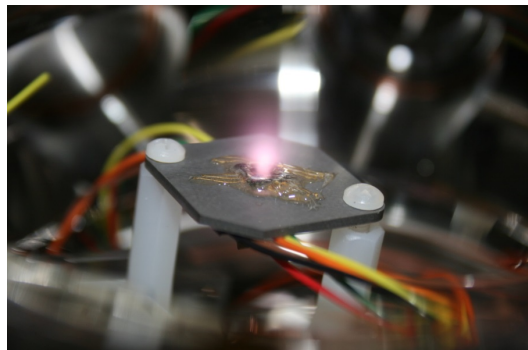
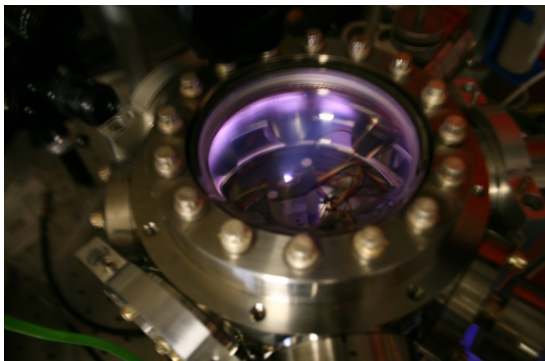
Stanford SR430 Multi-Channel Scaler

DEI PVX-4150 Pulse Generator

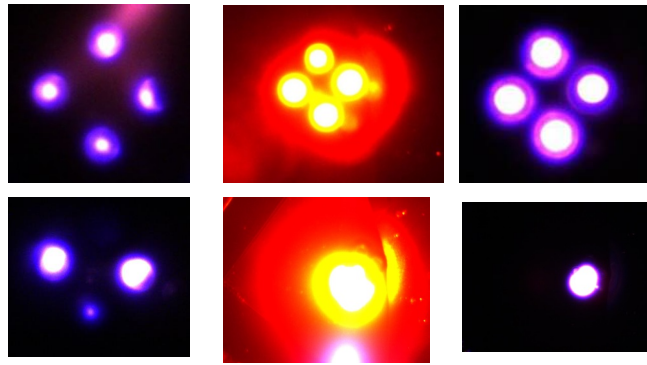
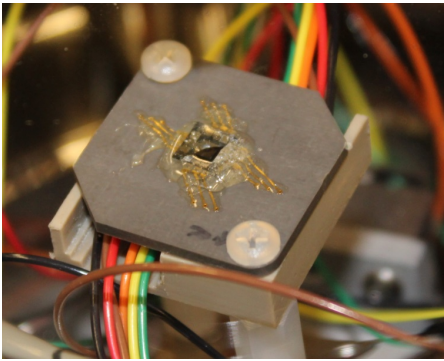
Amplifier Research 75A250A Amplifier

Various elements of the measurement system.

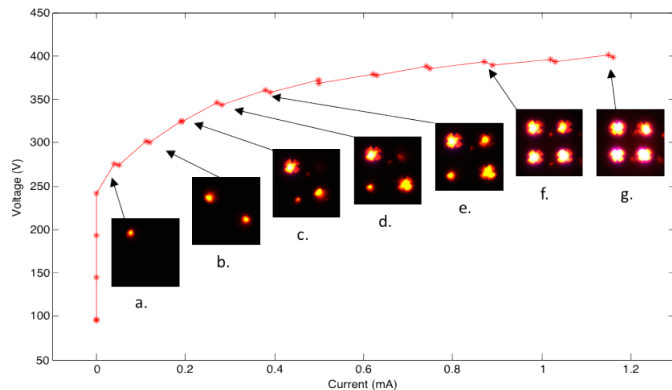
## A2.3 Assorted microplasma images



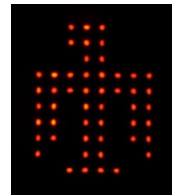
In initial experiments, pressure sensor failure caused inaccurate pressure readings. This was repaired in all subsequent measurements presented herein. Improper pressure and lack of shielding of surrounding grounded surfaces allowed plasma to extend to the test chamber walls (left). The image at right shows the extent of the plasma when external surfaces potentials are not properly shielded in the incorrect pressure regime.



The image at the left shows our first attempts to shield nearby grounds using epoxy on the chip edges and circuit board traces, as well as a machined PEEK back plane. At right are microplasma images of 4-element arrays of 100  $\mu\text{m}$  diameter MD. The images are with Ar, Ne and He, from left to right. With increased shielding, plasma confinement to the device region is improved. Further improvements in board design are shown in section A2.2.



A voltage-current plot with superimposed optical images showing that as the bias is increased sequentially more of the MD begin to discharge.



An array of 100  $\mu\text{m}$  diameter MD arranged in the shape of a Sandia Thunderbird ignited in Ne.



## **DISTRIBUTION**

4 Lawrence Livermore National Laboratory  
Attn: N. Dunipace (1)  
P.O. Box 808, MS L-795  
Livermore, CA 94551-0808

1	MS0386	Juan Elizondo-Decanini	2152
1	MS0889	Wahid Hermina	1850
1	MS1086	Mary Crawford	1100
1	MS1425	Steve Casalnuovo	6830

1 MS0899 Technical Library 9536 (electronic copy)

For LDRD reports, add:

1 MS0359 D. Chavez, LDRD Office 1911

For CRADA reports add:

1 MS0115 OFA/NFE Agreements 10012

For Patent Caution reports, add:

1 MS0161 Legal Technology Transfer Center 11500



**Sandia National Laboratories**